Numerical Investigation of the Use of Nanofluid in a Photovoltaic Thermal System

Nora Grebstad

Supervisor: Boris V. Balakin

Master's Programme in Energy with Specialization in
Mathematics, Physics and Informatics
Geophysical Institute
University of Bergen

June 1, 2022

Abstract

Despite the impressing development of solar technologies, there are still challenges with the energy efficiency of the existing devices. Solar photovoltaic panels suffer from low efficiency, one of the reasons being overheating. Combined photovoltaic thermal (PV/T) systems have been introduced as a solution to this obstacle in controlling the temperature of the solar cell and taking advantage of the excess heat generated in the panel. The most common PV/T system focuses on cooling the back of the photovoltaic panel. Another option is implementing fluid on top of the panel, directly absorbing the radiation that is harmful to the panel. Nevertheless, traditional heat transfer fluids exhibit overall poor thermal properties, limiting the thermal efficiency of conventional solar thermal systems. Therefore, the concept of dispersing nanoparticles into a base fluid has been introduced and proven to enhance several thermal and optical properties of a heat transfer fluid, providing the opportunity to increase the efficiency of the already existing solar collecting devices.

Since the first published paper, many researchers have studied the enhanced properties of nanofluids and how they improve different solar energy devices, especially solar collectors. Further research is needed for optical PV/T systems to obtain optimal energy efficiency, and is a motivation to the focus of this project. The objective of the study was to investigate a numerical model of an optical carbon-based nanofluid PV/T system using computational fluid dynamics software. The objective was to study how different operational conditions affected the system's efficiency. The focus variables were the optical fluid's extinction coefficient and the fluid mass flow rate. The following cases were studied: a standalone photovoltaic panel, water in the PV/T at mass flow rates of 1, 5, and 10 kg/min, and nanofluid in the PVT at concentrations of 0.003 to 0.08 wt. % at the same mass flow rates. The system was under constant radiation in all of the cases. The system's electrical, thermal, and total efficiencies were obtained in the simulation.

The results were compared to one another, and the effect of varying the different parameters were discussed. The highest total efficiency (57.6 %) of the system was achieved for the case with water in the PV/T system, with the mass flow rate set to 10 kg/min. It was observed that increasing the particle concentration resulted in a decreased electrical efficiency and an increased thermal efficiency. The results from the numerical simulations agree well with similar studies.

An additional experimental study was also performed, where the thermal

conductivity of prepared carbon black nanofluids was measured for concentrations 0.5 wt.% to 6 wt.%, where the objective was to study how the increasing particle concentration affected the thermal conductivity. This raises the potential to investigate the possibility of a high concentration nanofluid cooling the top of the panel, where the panel's temperature controls the mass flow. An enhancement of 7.38 % was achieved for the particle concentration of 4 wt.%. According to the results, increasing the concentration of nanoparticles yields an increasing thermal conductivity. Many similar studies in the literature support this correlation.

Acknowledgements

I want to express my sincerest appreciation and gratitude to my supervisors professor Boris V. Balakin from the Department of Mechanical and Marine Engineering at the Western Norway University of Applied Sciences and professor Pawel Jan Kosinski from the Department of Physics and Technology at the University of Bergen. Boris, I am grateful for your valuable guidance and advice throughout the process of this project. Pawel, thank you for your help and constructive advice on this thesis. Thank you both for always answering my many questions and concerns.

I also wish to thank Dr Pavel Struchalin from the Department of Mechanical and Marine Engineering at the Western Norway University of Applied Sciences, Patrice Estellé from Laboratoire de Génie Civil et Génie Mécanique (LGCGM) at Université de Rennes 1, and Sergey Anpilov from Department of Computational Methods at Moscow State University. Thank you, Pavel, for your assistance in teaching me how to prepare nanofluids and handle the laboratory equipment. Patrice, thank you for welcoming me to LGCGM to conduct experiments in your laboratory and for providing me with helpful advice. Thank you, Sergey, for giving me fundamental knowledge about the subject of computational fluid dynamics and the software STAR-CCM+.

I am also grateful for the invaluable support from my fellow master's students at the Department of Physics and Technology at the University of Bergen They have been crucial for my progress and motivation this last year. Especially Linna Nguyen, thank you for all the helpful and interesting discussion, as well as being a motivation in the master's office. Last but not least, I wish to show my appreciation to my dear family for being so understanding and caring. This would not have been possible without your support.

Nomenclature

Abbreviations

CNT Carbon nanotube

DASC Direct absorption solar collector

PV/T Photovoltaic thermal

SDS Sodium dodecyl sulfate

SWCNT/MWCNT Single/multi-walled carbon nanotube

Greek Letters

β	Solar cell temperature coefficient (%/K)
β	Tilt angle of plane (°)
δ	Fluid film thickness (m)
ϵ	Emissivity
η	Efficiency (%)
η_H	Dimensionless heat transfer number
Γ	Liquid loading (kg/ms)
λ	Wavelength (m)
μ	Dynamic viscosity (Pas)
ν_e	Kinematic viscosity (m^2/s)
ρ	Density (kg/m^3)
σ	Extinction coefficient (m^{-1})
σ	Stefan Boltzmann's constant ($5.669 \cdot 10^{-8}$ W/m^2K^4)
τ	Shear Stress (Pa)

Latin letters

ΔCB	Uncertainty of concentration of CB
Δk	Uncertainty of thermal conductivity (W/mK)
ΔSDS	Uncertainty of concentration of SDS
$\dot{m}$	Mass flow rate (kg/s)

$\mathbf{f}_b$	Body force per unit volume (N/m^3)
$\mathbf{T}$	Viscous stress tensor
$\mathbf{v}$	Velocity vector
A	Area (m^2)
c	Speed of light in vacuum ($2.998 \cdot 10^8$ m/s)
c_p	Specific heat capacity (J/kgK)
$c_{p,F}$	Specific heat capacity of fluid (J/kgK)
$c_{p,PV}$	Specific heat capacity of photovoltaic panel (J/kgK)
E	Energy (J)
e	Energy flux (W/m^2)
e	Enthalpy (J)
F_g	Gravitational Force (N)
F_{1-2}	View factor
g	Gravitational acceleration (m/s^2)
H	Total fluid enthalpy (J)
h	Heat transfer coefficient (W/m^2K)
h	Planck's constant ($6.626 \cdot 10^{-34}$ Js)
I	Intensity (W/m^2)
I_0	Incident intensity (W/m^2)
k	Thermal conductivity (W/mK)
k_{avg}	Average thermal conductivity (W/mK)
L	Length of plane (m)
m	Mass (kg)
n_{enh}	Enhancement (%)
Nu	Nusselt number
p	Pressure (Pa = kg/ms^2)
Pr	the Prandtl number

Q	Heat (J)
q	Heat flow rate (J/s)
q_0	Incident heat flux (W/m^2)
q_g	Heat generation rate in system (J/s)
q_{in}	Heat transfer rate into system (J/s)
q_{out}	Heat transfer rate out of system (J/s)
r	Fluid depth (m)
S_E	Energy source term per unit area (Jkg/sm^2)
s_m	Momentum source (kg/ms^2)
S_u	Mass source per unit area (kg/s^2)
T	Temperature (K)
T_s	Sonication time (min)
U	Internal energy (J)
u	Fluid velocity (m/s)
u_0	Inlet fluid velocity (m/s)
V	Volume (m^3)
W	Work (J)
x	Spatial coordinate (m)
y	Fluid depth (m)
y	Spatial coordinate (m)
z	Spatial coordinate (m)
Re	the Reynolds number

Subscripts

AMB	Ambient
b	Blackbody radiator
e	At the leading edge
f	Fluid

g	gravitational
IN	At fluid inlet
OUT	At fluid outlet
PV	Photovoltaic
PV, C	Photovoltaic, cooling
ref	Reference
th	Thermal
w	Wall

Contents

1 Introduction

1.1 Motivation

The world is facing an increasing energy demand. The global primary energy consumption in 1950 was about 28 516 TWh, facing a fivefold increase to 173 340 TWh in 2019. The share of fossil fuel in 1950 was 71 % of the consumption, while in 2019, the share increased to 79 % [1]. Figure 1 shows how the global primary energy consumption by source since the year 1800 and up to 2019, reproduced from [2]. The Covid-19 pandemic has impacted the energy picture in the last years, partly due to the uneven economic rises and falls. For example, in 2021, the electricity demand faced a slight decrease of 1 % [3]. Coal and oil use experienced a considerable rebound in 2021, contributing to the second-largest annual rise in CO_2 emission in history [4].

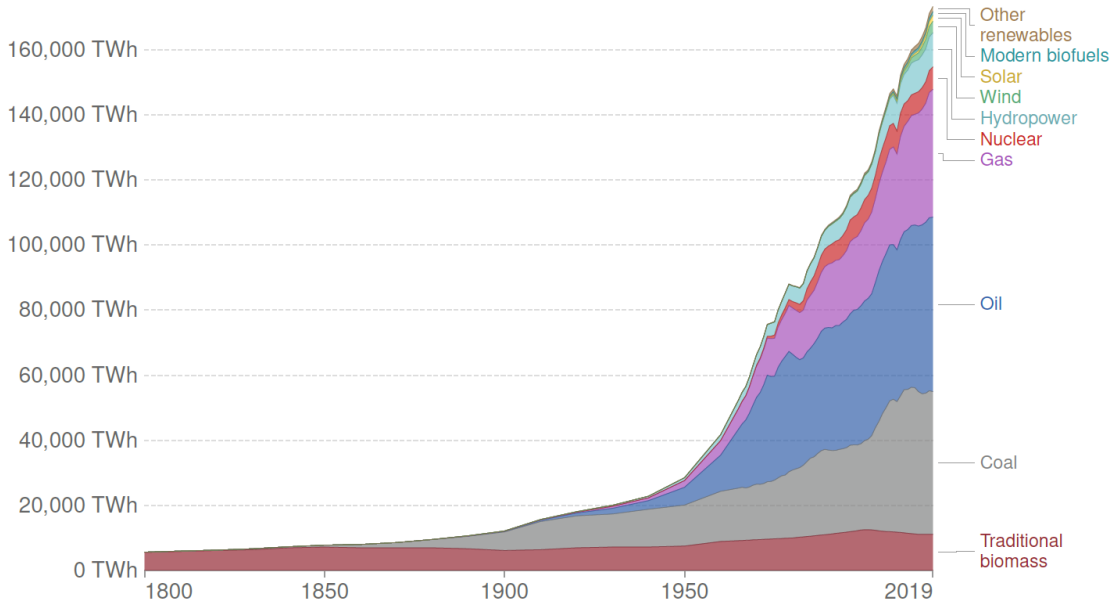

Figure 1: Global primary energy consumption by source, reproduced from [2]

Despite this temporal decrease, the energy demand is predicted to rise by 4 % in 2022. Followed by these predictions, almost half of this demand will be covered by fossil fuels, where coal accounts for the most significant portion. This threatens to push the CO_2 emissions to record levels in 2022. Renewables are predicted to rise by 6 % in 2022. However, this is not sufficient to compensate for the rapid increase in electricity demand and will only be

able to cover half of it. Fossil fuels are predicted to cover about 40 % of the additional demand in 2022, with nuclear power covering the rest [3]. In other words, renewables are not growing fast enough to keep up with the rising electricity demand.

The UN Climate Change Conference (COP21) in Paris resulted in the Paris Agreement in 2015, aiming to reduce emissions in order to limit the temperature increase of the century to 2 °C, with an ideal limitation of 1.5 °C. Each country participating vowed to update its climate action plan every five years. All the agreement details were finalized at the Climate Change Conference (COP26) in Glasgow in 2021. The global average temperatures increased by 1.1 °C since the pre-industrial age, with the emissions from the energy sector being the major contributor. The world population is predicted to grow by around 2 billion by 2050, and the current energy system cannot meet the increasing energy and technology demand while also satisfying the climate goals. In the "World Energy Outlook 2021" report [4], it is stated that the solar photovoltaic energy generation needs to see a more rapid growth than the announced pledges state if the climate goals are to be satisfied.

There are still significant gaps to fill in energy technology to satisfy the 1.5 °C Paris climate objectives, and the world should achieve net zero emissions by 2050 to reach them. This is an immense motivation for the heavy competition conventional energy sources (for instance, oil, coal, and gas) are receiving from non-conventional sources [5]. The global energy consumption would be required to be reduced by 11 % from 2019, along with an increase in renewables to reach a 79 % share. In comparison, the renewable share was 19 % in 2019. To achieve this, renewables' energy efficiency needs to significantly improve in the following years, making countries less dependent on imported fossil fuel energy. A positive note is that renewable energy production costs continue to decrease [6].

The sun is the most abundant energy source available to the earth. The solar radiation reaching the earth's surface in an hour and a half carries enough energy to cover the global energy consumption for an entire year [7]. The sun radiates electromagnetic waves, where wavelengths incident upon the earth's surface range from about 300 to 2500 nm, including the radiation containing the most energy (300 – 1100 nm) and the near-infrared spectrum (1000 – 2500 nm) [8]. Figure 2 is reproduced from [8] and displays the electromagnetic spectrum and which parts of it that occur in solar radiation.

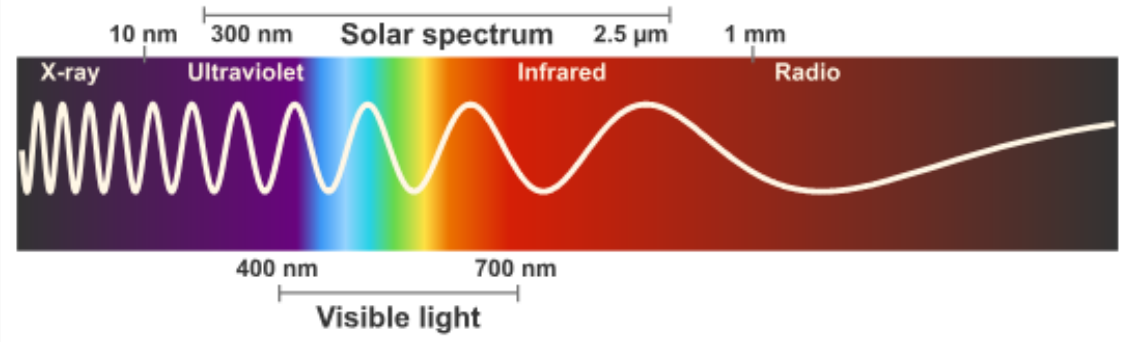

Figure 2: Electromagnetic Spectrum, reproduced from [8]

Solar technologies aim to convert solar energy into electrical and thermal energy. The existing devices for this purpose are photovoltaic panels and solar collecting devices [7]. From 2011 to 2021, the global installed solar energy capacity increased from 72 921 MW to 849 473 MW. Solar photovoltaics account for most of this, whereas solar thermal installation only contributes by 0.8 %. This is partly due to the accelerating installation of cheap solar photovoltaics worldwide [9].

Solar photovoltaics is currently, after wind, the cheapest energy technology worldwide. The technology in these areas is growing rapidly, and the clean energy sector is expanding in investment and employment [4]. One reason for this is the increasing demand for renewable energy, resulting from the climate challenges the world is experiencing [10].

Despite the rapidly increasing solar energy technology, there are still a few energy efficiency challenges. Today's commercial devices fail to efficiently transform the energy of solar radiation into more useful energy forms. There are many obstacles to both photovoltaics and solar collectors [11]. A known problem with photovoltaics is the temperature-dependent performance. For most solar cells, the electrical efficiency decreases significantly when the cell temperature increases [12]. Another major drawback to solar photovoltaics is that only a small range of wavelengths from the incoming radiation is useful for generating electrical energy. It varies for different materials, but for most silicon cells, the effective range for generating electrical energy is between 700 and 1100 nm [13]. The remaining energy is rejected as heat within the panel, dissipating to the surroundings or heating the panel [14].

There are different types of solar collectors, and conventional surface collectors depend on surface absorption. Here, there are several required steps of heat transfer to harvest the energy. The system is therefore exposed to sig-

nificant heat loss during the process, partially due to the thermal resistance between the surface absorber and the heat transfer fluid. A direct absorption solar collector (DASC) removes this obstacle, where the radiation is absorbed directly within the fluid. Therefore, the heat transfer steps between the absorbing surface and the heat transfer fluid are avoided. There is not as much heat loss to the environment because the surface exposed to the environment does not hold a notably high temperature [15].

Photovoltaic thermal systems combine the two groups of solar technology and generate electrical and thermal energy. The radiation with energy levels outside the photovoltaic bandgap is either reflected or absorbed by the panel, where the absorbed radiation generates heat. The most successful solution to this problem is cooling by air or water. Without actively cooling the panel, the temperature can increase by 1.8 °C for every 100 W/m^2 [14].

There are two main types of PV/T systems, and figure 3 shows a sketch of the concept of them. The first and most common type consists of a photovoltaic solar cell with a heat transfer fluid system behind it to harvest the excess heat from the photovoltaic panel. Water is the most frequently used fluid for this matter. The second type consists of a solar cell covered by an optical fluid that is supposed to selectively transmit useful radiation to the solar cell. The other radiation is either reflected or absorbed by the fluid [13].

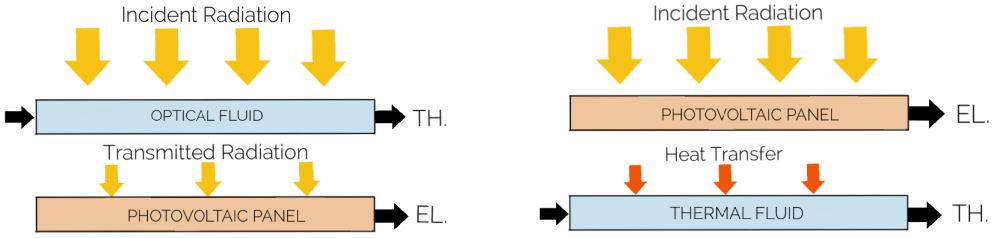

Figure 3: Conceptual sketch of both thermal and optical PV/T system (EL. and TH. denotes electrical and thermal energy, respectively)

It was Martin Wolf [16] who first studied the performance of a flat plate PV/T system for residential application in 1976. For countries with low solar radiation and a cold climate, the PV/T system can be used to cool the photovoltaic device and heat space. In warmer areas, they can be more suited for residential water heating [17]. PV/T systems prevent the photovoltaic

panel from being damaged by thermal stress by controlling the working temperature of the panel and extending its service life. They are also more space- and cost-effective and increase the overall efficiency. Application of PV/T on a small scale can be used for water distillation, while the large-scale application can supply energy to households [18].

Conventional heat transfer fluids like water, oils, and glycols have been frequently used in generating power, electronics, air-conditioning systems, chemical production, nuclear power, space and defense, transport, microelectronics, and other heat transfer processes [19]. However, these fluids exhibit relatively poor thermal properties, especially compared to solids [20]. Therefore, the objective to enhance the thermal properties of heat transfer fluids has become a widely studied subject.

The concept of dispersing nanoparticles in a fluid to enhance the heat transfer properties was first introduced by Choi [21] in 1995. Before, microsized particles were used and researched. The large size of the particles, however, led to comprehensive problems like clogging and corrosion. Choi introduced a solution to these problems: nanosized particles dispersed in a base fluid, referred to as nanofluids. Their impressive optical and thermal properties have sparked broad interest in the application of nanofluids in several engineering fields [19].

When it comes to heat transfer of fluid, thermal conductivity is an important property. It is the fluid's ability to conduct heat [22]. Dispersing nanoparticles into a base fluid is known to enhance the thermal conductivity of the fluid, and thus the performance of a thermal system ([22], [5], [19], [21], [23], [24]).

Since the first published article, the nanofluid area has received increasing attention and research, leading to over 2000 published papers by 2022. The subject of nanofluids has mainly been studied in the academic fields of engineering, physics, chemical engineering, and materials science. The list of potential applications for nanofluids continues. Some of the most popular applications are solar collectors, photovoltaic systems, car radiators, refrigerators, boilers, medicine-drug delivery, cooling of electronic equipment, lubrication of components, heating and cooling of buildings, desalination, CO_2 absorption, porous media, aerospace, oil recovery and any liquid-based heat exchanger [25].

1.2 Specific Objectives

The objective of this project was to numerically study an optical PV/T system for different cases using computational fluid dynamics software. The

photovoltaic panel was simulated alone, and the PV/T system was simulated for the cases corresponding to using carbon-based nanofluid at concentrations 0 wt.% to 0.08 wt.%. This was done by varying the extinction coefficient in the simulation file. For each concentration, the mass flow rate of the system was varied between 1 kg/min and 10 kg/min. In the simulation, the system's thermal, electrical, and total efficiencies were calculated. These results were later compared and discussed against the literature.

The objective of the additional experimental part of this project was to prepare carbon black nanofluid at different particle concentrations, followed by measuring their thermal conductivity. Concentrations of 0.5 wt.% to 6 wt.% were prepared, and the transient hot-wire method was used for the measurements. The results were discussed and compared to the literature.

2 Theory

2.1 Nanoparticles and Nanofluids

Nanoparticles are small particles whose size is less than 100 nm. The most commonly used nanoparticles range from 10 to 50 nm in diameter [26]. A nanofluid is a result of dispersing nanoparticles into a base fluid. It has been found that carbon-based materials and metals are the most successful materials because they are cost-effective and highly absorptive, which are valuable qualities of a nanofluid. Water is a frequently used base fluid in different nanofluids [26]. Nanofluids have proven to exhibit impressive heat transfer characteristics and have therefore become the subject of many studies since the first published article in 1995 by Choi [21].

A fluid's ability to absorb sunlight can significantly increase by inserting nanoparticles. The absorption process depends on the material, size, shape, and volume fraction of the nanoparticles [27]. For volume concentrations $<$ 1 %, nanoparticles can lead to enhanced thermal properties, but the photothermal conversion dominates when the concentration becomes very low. It is, however, crucial to choose the suitable nanoparticle material for the application of interest, or there is a risk of negatively affected properties of the fluid [27]. Under the right circumstances, nanofluids can enhance the convective, conductive, and radiative heat transfer, not the least photothermal conversion. Extensive enhancement can be achieved without any significant increase in pumping power. These characteristics make nanofluids promising in large and small-scale solar collection and heat transfer systems. Nanoparticles also exhibit qualities that could enhance the phase change process in a nanofluid by volumetric light absorption [27]. The enhancement of heat transfer is dependent on several factors, such as an increase in thermal conductivity, the chaotic movement of the nanoparticles, fluctuations, and interactions [20]. Through experimentation, researchers have concluded that adding nanoparticles to a base fluid increases thermal conductivity and viscosity. Although to obtain the best results, it is a prerequisite that the nanofluid is stable [25]. This can be achieved by adding some specific steps to the preparation process described later in this chapter.

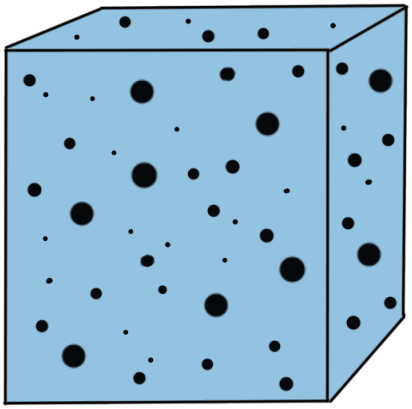

Figure 4: Nanofluid sketch

Figure 4 shows a conceptual drawing of a nanofluid. Materials that have been frequently investigated in nanofluids are metals such as aluminium (Al), copper (Cu), gold (Au), silver (Ag), single- and multi-walled carbon nanotubes (SWCNT/MWCNT) [19], carbon black particles [28], and graphene [22]. Heris et al. [20] investigated the convective heat transfer of copper oxide (CuO) and aluminium oxide (Al_2O_3) dispersed in water in laminar flow. They observed an increased heat transfer coefficient when increasing the particle concentration in the nanofluid. Several studies have been performed for Al_2O_3 nanoparticles dispersed in water and used in flat-plate solar collectors ([29], [30], [31]). Crisostomo et al. [32] studied core-shell Ag-SiO_2 nanoparticles dispersed in water as an optical filter on top of a photovoltaic panel. Hjerrild et al. [33] also analyzed Ag-SiO_2 for the same purpose but extended their research by comparing with carbon nanotubes. Abdelrazik et al. [34] investigated silver in a water-based nanofluid for optical filtering in a similar PV/T system. Al-Shamani et al. [35] investigated SiO_2 nanofluid for a tubular PV/T system. Abdallah et al. [36] studied low concentration MWCNT nanofluid, also for PV/T application. Struchalin et al. [37] also researched the performance of MWCNT nanofluid, but for use in a tubular direct absorption solar collector (DASC).

As mentioned in Chapter 1.1, there are two ways of using a fluid in a PV/T system. Some materials are efficient to exploit in thermal nanofluids for broadband absorption, mostly pure materials. The most successful materials for optical filtering are semiconductors, metals, and core-shell composite

nanoparticles [38]. The core-shell particles consist of a core and a shell of different materials. The radius ratio between them can be optimized to achieve the desired optical properties of the particles. The most frequently used optical nanoparticles in the literature are core-shell Ag-SiO_2 ([34], [32], [33]), all yielding good results for filtering desired wavelengths. Taylor et al. [38] studied core-shell noble metals and silica (Si) nanofluids as an optical filter in a PV/T, using aluminium (Al), gold (Au), and silver (Ag). Core-shell particles are cost-effective because the amount of material needed is less than that for pure materials [38]. Semiconductor nanoparticles absorb and transmit radiation in ranges similar to photovoltaic cells and are therefore efficient in these optical PV/T systems [38]. Metals have a natural frequency called the *plasmon peak*, where they experience a peak in the absorption and oscillation of the electrons inside the metal. This peak is usually found at wavelengths between 0.2 and 0.5 μm [26]. Due to their resistance to corrosion and oxidation, noble metals are the best alternative for this case [38].

It is essential to obtain a stable nanofluid for experiments and heat transfer applications. If the nanofluid is not stable, there will be agglomerates and sediment, changing the fluid's thermal properties. This can lead to malfunctions when used in a system and incorrect measurement values [26]. Many researchers have studied how to obtain stable nanofluids, where the method for achieving this depends on the material and concentration. Two main methods are often used for nanofluid preparation: a one-step and a two-step process. The one-step method involves achieving the desired particle size and volume fraction by synthesizing the particles inside the base fluid. On the other hand, with the two-step method, the particles are synthesized to their intended shape before being dispersed in the base fluid. Often some additives are applied to increase the stability. Research shows that the one-step method might be the most successful if it is possible to implement on a large scale without a significant cost [26]. In this project, the two-step method is used.

The two-step process may take from a few minutes up to several hours, depending on the stability and quality needed for the application. The stability additive that is used also varies, depending on the application. Taylor et al. [26] studied the solar absorption in nanofluid and compared the results to model predictions. In this case, extremely low volume fractions ($<$ 0.001 %) of nanoparticles and about 1% of sodium dodecyl were dispersed into the base fluid and sonicated for 15 to 30 min. It was discovered that a probe sonicator outperformed a bath sonicator in this case. When investigating the performance of carbon black nanofluids, Kosinska et al. [39] mixed the particles in water and sodium dodecyl sulfate (SDS). The suspension

was mixed with a magnetic stirrer for 20 minutes before being placed in an ultrasonic bath for 1 hour. Concentrations from 0.25 to 1 wt.% were prepared. This method has proved to be successful in other research as well ([40], [41], [42], [43], [28], [44]). Some surfactants that are frequently used in carbon-based aqueous nanofluids are sodium dodecyl benzene sulfonate (SDBS), sodium dodecyl sulfate (SDS), and dodecyl betaine (DB). These surfactants prove to obtain long-term stable solutions and increase thermal properties. Sedong et al. [45] did an experimental study concluding that SDS was the most suitable surfactant for carbon-based nanofluids. This surfactant yielded the highest achieved thermal conductivity. Struchalin et al. [37] achieved high stability in the prepared nanofluids, where no visible deposition of particles was observed for at least 45 days. In this case, the base fluid consisted of water, 10 wt.% ethanol, and defoamer, which was applied after the dispersion process. The downside with surfactant stabilized nanofluids is that they tend to break down under increasing temperature. One option is to re-sonicate the nanofluid to maintain the stability; another is to investigate more advanced methods [26].

Verma et al. [5] concluded that particle concentration is an essential parameter for the resulting efficiency of solar collectors. An advantage of nanoparticles is the low concentration required to achieve a significant increase in efficiency, and the risk of clogging is low. According to Taylor et al. [26], an optimum particle concentration can be found for each nanofluid in a solar collector. At very low concentrations, increasing the concentration will also increase the thermal efficiency up to the optimum concentration. Beyond this concentration, the nanofluid will gradually act more and more like a surface absorber due to the increasing abundance of particles at the top layer of the nanofluid. As mentioned, surface absorbers suffer from high heat loss due to the high temperature and direct contact with the surrounding air. The mass flow rate will have to be increased to avoid this heat loss. This means a higher pumping power is needed; hence the system becomes more expensive [19]. Struchalin et al. [37] discovered an optimum concentration of 0.01 wt.% multi-walled carbon nanotubes in a tubular DASC. Otanicar et al. [46] found the optimum concentration of silver nanoparticles dispersed in water to be 0.25 wt.% in a volumetric absorber, enhancing the thermal efficiency by 7 % compared to a conventional surface absorber. Karami et al. [47] found the optimum concentration of copper oxide nanofluid to be 0.01 wt.% in a DASC, where the highest thermal efficiency was achieved.

Water is, as earlier mentioned, the most commonly used base fluid in heat transfer applications. Also, Therminol VP-1 is a commonly used base fluid. This heat transfer fluid is used a lot for solar collectors. The liquid has a

slightly higher viscosity than water and has no color. Its boiling point is at 257°C, which makes it ideal for medium-temperature collectors. Compared to water, this base fluid is less dominant of an absorber at the longer wavelengths [26]. Sharaf et al. [15] studied the effect of the base fluid in a nanofluid DASC. For particle volume concentrations up to 0.005 %, water-based nanofluids were more efficient than therminol-based ones, while therminol-based nanofluids were the best solar absorbers for higher particle concentrations.

Carbon is a frequently used and studied material for nanofluids. This is among others due to its high radiation absorption, high thermal conductivity, strength, and large surface area [19]. Carbon-based nanofluids are relatively easy and inexpensive to produce [28], which is another advantage of using these particles for large-scale applications. Hwang et al. [48] concluded that multi-walled carbon nanotube nanofluids display a higher thermal conductivity than other investigated nanofluids. This can be explained by the high thermal conductivity of the particles. For low particle concentrations (< 0.1 wt.%) of carbon-based nanofluids, the thermal properties can be assumed to be the same as for water [37]. In this case, only the optical properties of the fluid are different from water, such as absorption, reflection, and scattering.

In their study, Struchalin et al. [37] achieved the highest average efficiency of the collector at 80 %. Compared to a traditional opaque surface solar collector, the volumetric collector gained up to 37.9 % higher thermal efficiency. They also discovered that increasing the system's flow rate led to a decrease in fluid heating, which can be understood because the fluid is present in the collector for a shorter amount of time. The carbon-based particles yielded the highest thermal efficiency compared to other materials from the literature. In addition, they could prove a higher thermal efficiency of the DASC when using carbon-based nanofluid than water. Kosinska et al. [28] used spherical carbon nanoparticles (Timcal Enasco 350g) in their study, with concentrations 0.5 – 2 wt.%. The thermal performance of the nanofluid was investigated, and the maximum thermal efficiency was discovered to be 16 % higher than that of pure water. Yang et al. [49] measured the convective heat transfer of graphite nanofluids under laminar flow in a horizontal tube heat exchanger. The results proved that the nanoparticles increased the heat transfer coefficient of the system. Bester [50] researched carbon black nanofluid in concentrated solar power applications. Through experiment, they found an optimum volume concentration of 0.001 %, where the heating rate faced an increase of 42 % compared to the base fluid, which in this case was saltwater. However, due to severe thermal losses, the maximum effi-

ciency of the collector resulted in being only 23 % higher than that of the base fluid. The high thermal losses can explain this due to high temperatures in the collector. Yang et al. [49] used graphite, Li et al. [51] investigated carbon nanotubes (CNT), and Hamze [22] did experimental research on few-layer graphene (FLG) particles. These different carbon-based nanosized particles will differ in performance in nanofluid application because they have different sizes, densities, surface areas, purity levels, and geometry. These properties will affect the resulting nanofluid's thermal conductivity, viscosity, absorption, and specific heat.

Even though nanofluids show promising thermal properties and potential in many applications and industrial areas, there are some drawbacks. Different nanofluid materials can be very hazardous to living creatures and the environment and expensive to produce. Because of the toxicity of many of the materials, nanofluids might not be suitable for, for example, water purification. They can also impose problems in complex geometrical systems, like clogging, deposition, and erosion. This problem can, as mentioned, be somewhat avoided by adding stabilizing additives [28].

2.2 Gravity-Driven Film Flow

Thin gravity-driven film flow along an inclined plane is described by mathematical analysis in [52]. The flow is assumed to be steady, laminar, with constant thickness and fully developed velocity gradients on a surface free of ripples. In addition, there is assumed to be no pressure drop along the plane, and the drag at the free surface of the liquid is considered so small that the shear stress here is ignored.

Figure 5 illustrates a fluid element in this type of flow, reproduced from [52]. In the figure, β is the angle of tilt, b is the layer width, δ is the thickness of the fluid layer, L is length of the fluid element, r is the thickness of the control volume element, F_g is the gravity force, and τA is the shear force on the lower surface of the element.

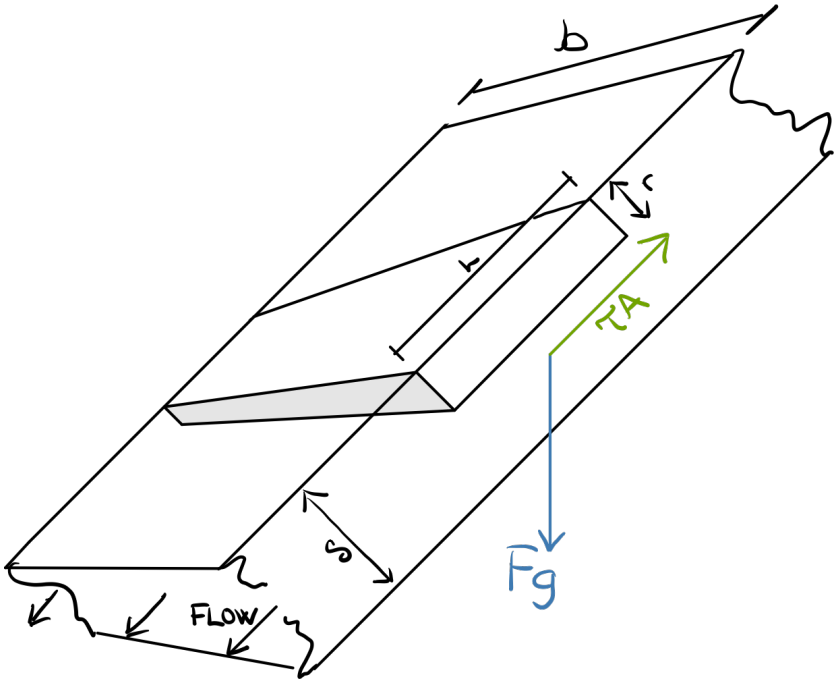

Figure 5: Thin fluid film flow on an inclined plane

From the model assumptions, a mathematical relation for the velocity profile of the flow can be derived. The assumption of steady flow requires the sum of the forces parallel to the flow to equal zero. As seen in figure 5, this is the sum of the sheer force τA at the bottom of the fluid layer and the parallel gravity component of F_g. This force balance results in:

$$F_g cos\beta - \tau A = 0. \tag{1}$$

With some manipulation of equation (1), the resulting velocity distribution in the layer is:

$$u = \frac{\rho g cos\beta}{2\mu}(\delta^2 - r^2). \tag{2}$$

Figure 6 illustrates the velocity boundary layer and the parabolic behavior of the velocity in the thin fluid layer.

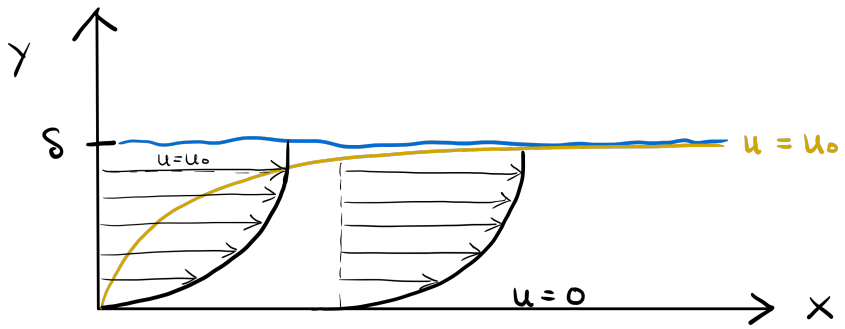

Figure 6: Velocity profile in a thin fluid film flow

If the fluid element has a cross section dS, the differential mass flow rate is:

$$\mathrm{d}\dot{m} = \rho u \mathrm{d}S = \rho u b \mathrm{d}r, \tag{3}$$

where dr is the thickness off the differential volume element. Integrating both sides of equation (3) gives the formula for the mass flow rate:

$$\dot{m} = \int_0^{\delta} \rho u b \mathrm{d}r = \frac{b\delta^3 \rho^2 g cos\beta}{3\mu}. \tag{4}$$

Solving equation (4) results in the mathematical expression for the fluid flow film thickness:

$$\delta = (\frac{3\mu\Gamma}{\rho^2 g cos\beta})^{1/3}, \tag{5}$$

where Γ is the liquid loading $\frac{\dot{m}}{b}$ [52].

When dealing with fluid dynamics, the Reynolds number is a significant dimensionless number. The number decides whether the flow is laminar, turbulent, or partially laminar and turbulent [52]. The Reynolds number for a flat plate thin film flow depends upon the inlet velocity u_0, the fluid film thickness δ, the fluid density ρ, and the viscosity μ. It is expressed as

$$Re = \frac{u_0 \delta \rho}{\mu}. \tag{6}$$

For most simple fluid flow cases, Reynolds numbers below 2100 are associated with a fully laminar flow. For Reynolds numbers between 2100 and 4000, there is a transition region, where the flow can be either laminar or turbulent at a point. Ordinarily, Reynolds numbers above 4000 indicate that the flow is fully turbulent.

2.3 Thermal Physics

2.3.1 Heat Transfer

Heat transfer is a process where energy is transferred due to a temperature difference. In all cases, heat flows to a region of lower temperature than the source region. There are three basic modes of heat transfer: conduction, convection, and radiation [53].

Conduction

Conduction is a mode of heat transfer where heat flows without any motion of matter and is driven by a temperature gradient. On a small scale, the heat transfer happens at a molecular level, where molecules in a fluid collide. Energy and momentum are transferred from high-energy molecules to molecules of lower energy. This happens because regions of high temperature contain molecules of high energy and the opposite. There is a proportionality relation between the heat flux and the gradient, which according to to [53] can be presented as:

$$\frac{\mathrm{d}q}{\mathrm{d}A} = -k\frac{\partial T}{\partial x} + \frac{\partial T}{\partial y} + \frac{\partial T}{\partial z} = -k\nabla T, \tag{7}$$

where the left side represents the heat flux normal to the surface, k is the thermal conductivity, and ∇T is the temperature gradient in the spatial directions x, y and z. The thermal conductivity property is characteristic of each material. The negative sign in equation (7) can be explained by the fact that heat always flows in the direction of decreasing temperature [53].

Convection

Convection is the heat transfer mode where heat is transferred to the fluid in motion from a boundary surface. There are two types of convection: *forced convection* and *natural convection*. Figure 7 illustrates convective heat transfer due to a fluid flowing past a plate.

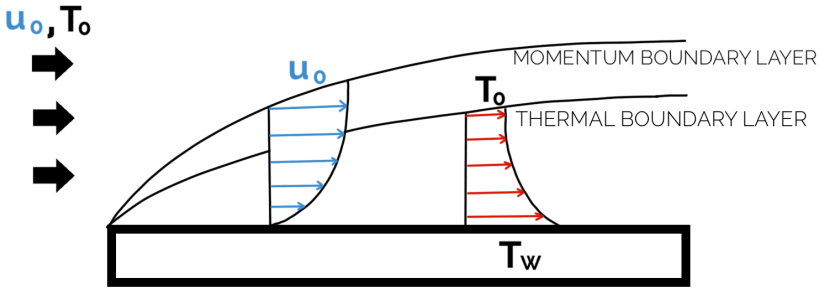

Figure 7: Illustration of forced convection over a plat plate

Forced convection refers to the case when a pump or a similar device induces the fluid flow. In contrast, natural convection occurs due to density differences caused by a temperature gradient. Even though the motion of fluid drives the convection process, the actual process occurring on a smaller scale is conduction within the moving fluid. In other words, the internal energy is transferred within the fluid.

When considering convective processes where heat is transferred from a boundary surface to a fluid with relatively low average velocity, an important property to introduce is the *heat transfer coefficient* h. The property is presented in *Newton's law of cooling*, expressed as:

$$\frac{q}{A} = h(T_w - T_f), \tag{8}$$

where q is the heat flow rate, A is the bounding surface area, T_w is the temperature of the wall, and T_f is the characteristic temperature of the fluid. T_f is often considered the enthalpy-mixed-mean temperature, the temperature the fluid will reach if it is stirred into a constant temperature. The heat transfer coefficient h highly depends on geometry, physical fluid properties, and fluid velocity [53].

According to the no-slip condition, heat transfer is due to conduction because the velocity is zero at the wall for a fluid flowing over it. Therefore, at the wall, equation (7) is the one accounting for heat transfer. By combining Fourier's law with Newton's law of cooling, the heat transfer coefficient is expressed as

$$h = \frac{q/A}{T_w - T_f} = -\frac{k(\delta T/\delta y)|_{y=0}}{T_w - T_f}. \tag{9}$$

An important dimensionless number in heat transfer is the Prandtl number, defined as the ratio between the momentum and thermal diffusivity. Physically, this describes how fast heat is transferred relative to how quickly momentum is transferred. If $Pr < 1$, heat is transferred more rapidly than momentum in the fluid, $Pr = 1$ means the thermal and velocity boundary layers are of the same thickness. Lastly, if $Pr > 1$, heat is transferred slower than momentum, which is the case for high viscosity fluids like oil [52]. For laminar flow over a flat plate, the Prandtl number of the fluid is:

$$Pr = \frac{c_p \mu}{k}, \tag{10}$$

where c_p is the fluid's specific heat, deciding how much energy is needed to increase 1 kg of the fluid by 1 K, μ is the fluid's viscosity, and k is the thermal conductivity.

The Nusselt number is also an important dimensionless variable. Physically, it signifies the ratio of convective heat transfer to conductive heat transfer in the fluid film. In heat transfer for flow over a flat plate, the average Nusselt number over the entire plate is:

$$Nu = \frac{hL}{k}, \tag{11}$$

where L is the distance from the inlet of the flat plate to the outlet. h is the average heat transfer coefficient over the entire plate, and for laminar flow, [53] expresses this constant as:

$$h = \frac{k}{L} 0.664 \sqrt[3]{Pr} \sqrt{Re} = \frac{k}{L} 0.664 \sqrt[3]{\frac{c_p \mu}{k}} \sqrt{\frac{u_0 \delta \rho}{\mu}}, \tag{12}$$

where δ is the film thickness, ρ is the density, and u_0 is the inlet velocity. Equation (12) only holds for Prandtl numbers greater than or equal to 1.0 and a Nusselt number higher than or equal to 10 [53].

Radiation

Thermal radiation is electromagnetic radiation emitted from a body, and the energy flux depends highly on the object's temperature. The radiation wavelength can range from 0.1 to 100 μm, and all objects with temperatures above 0 K emit thermal radiation. Radiation heat transfer does not require any medium to travel through; the most efficient heat transfer occurs in a vacuum. For a blackbody, an object emitting the same amount of energy as it absorbs, the energy flux emitted is expressed by the *Stefan Boltzmann's law*:

$$e_b = \sigma T^4, \tag{13}$$

where the Stefan Boltzmann's constant $\sigma = 5.669 \cdot 10^{-8}$ W/m^{2}K^4. Equation (13) only holds for an ideal radiator, and engineering surfaces generally do not perform as ideal radiators [53]. In this case, equation (13) is modified to:

$$e = \epsilon \sigma T^4, \tag{14}$$

where ϵ is the emissivity of the surface of the body and holds a value between 0 and 1. In the case where there is heat exchange by radiation between two blackbodies 1 and 2, the net heat exchange from 1 to 2 is expressed as:

$$q = \sigma A_1 (T_1^4 - T_2^4), \tag{15}$$

where T_1 is the temperature of body 1, and T_2 is the temperature of body 2. When only a fraction of the radiation from body 1 hits body 2, equation (15) becomes:

$$q = \epsilon \sigma A_1 F_{1-2} (T_1^4 - T_2^4), \tag{16}$$

where the *view factor* F_{1-2} is the value of this fraction. For real bodies, the view factor also depends on the emissivity of the bodies as well as the geometric view.

Solar Absorption in a Fluid

Solar radiation is another term for electromagnetic waves, which are emitted from the sun [54]. The energy of an electromagnetic wave is inverse proportional to the wavelength:

$$E = \frac{hc}{\lambda}, \tag{17}$$

Where $h = 6.626 \cdot 10^{-34}$ Js is Planck's constant, $c = 2.998 \cdot 10^{8}$ m/s is the speed of light in vacuum and λ is the wavelength of the electromagnetic wave [55]. The solar radiation at the earth's surface is often measured in W/m^2, which is referred to as the *intensity* of solar radiation [54]. The radiation incident on the surface of the earth holds wavelengths between 300 and 2500 nm, as seen in figure 2.

Figure 8 is reproduced from [56] and shows the solar AM1.5 direct normal radiation, which is a representation of the direct solar radiation reaching the surface in the areas with the highest level of incident sunlight. The figure shows a sharp peak in radiation in the visible spectrum (400 - 700 nm).

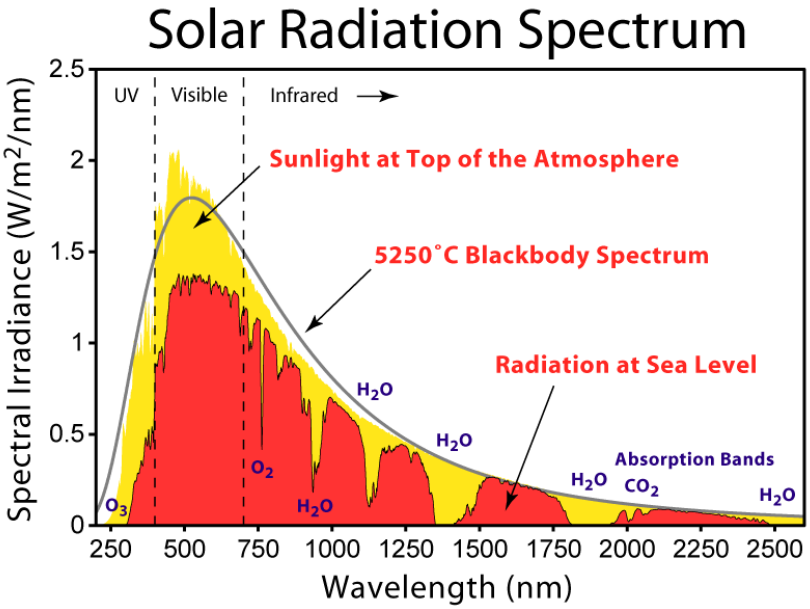

Figure 8: Solar Radiation Spectrum, reproduced from [56]

The principle of using particles to harvest solar energy was first officially studied by Hunt [57] in 1978, and later by Andresen et al. [58] in 1988.

Since then, particle-gas absorbing mixtures have been extensively applied for radiation heat absorption [27]. The thickness and extinction coefficient of a fluid decides how radiation intensity attenuates as it travels through the fluid. The extinction coefficient accounts for scattering and absorption within the fluid. Beer-Lambert's law is often used to decide the amount of heat that is absorbed in a nanofluid ([39], [37], [43]) and is illustrated in figure 10. Beer-Lambert's law describes the radiation that is still present at a given depth in the fluid compared with the incoming radiation and is defined as:

$$\frac{I}{I_0} = \exp(-\sigma y), \tag{18}$$

where σ is the extinction coefficient of the fluid, and y is the fluid depth where the radiation intensity I is considered. I_0 is the intensity of the incoming direct radiation [26]. Figure 9 shows a sketch of solar absorption in a nanofluid.

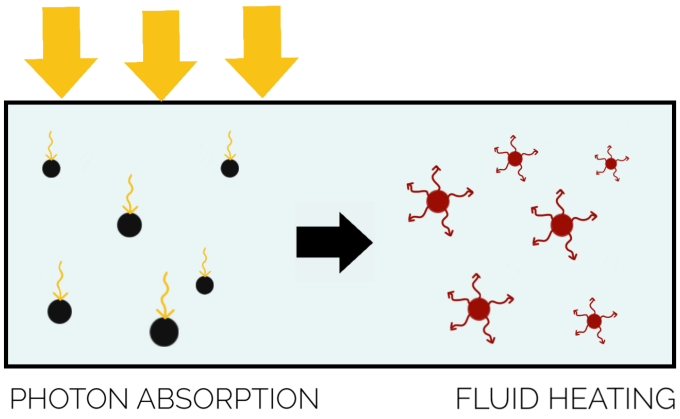

Figure 9: Sketch of solar radiation being absorbed by nanoparticles in a nanofluid

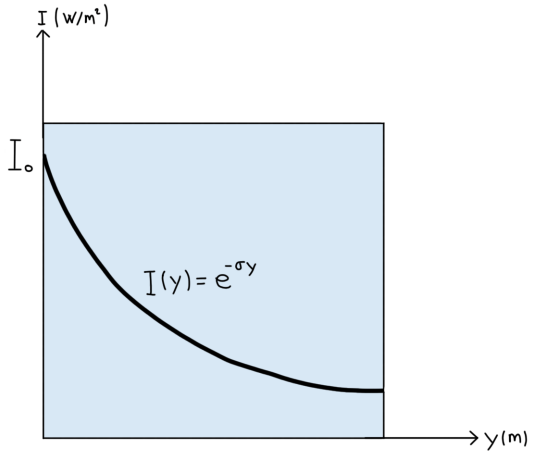

Figure 10: Sketch of the dissipation of radiation travelling through a fluid

For very low particle concentrations, it can be proven that the scattering in a nanofluid can often be neglected when calculating the extinction coefficient. This is because the nanofluid has a much higher absorption efficiency than scattering efficiency due to the low concentration and small particles with large gaps in between them [19, 26].

In reality, the nanoparticles will experience some level of agglomeration with a two-step preparation method. If the manufacturer's average particle diameter is between 20 and 40 nm, the real value can range from 50 to 120 nm. Because a slight change of the diameter can increase the scattering intensity significantly [15], it should be accounted for when particle agglomeration occurs [26]. With a nominal particle size of 100 nm, as much as 5 % of the incoming light can be scattered by a nanofluid. However, if the average particle size is < 50 nm, any potential scattering can be neglected for volume fractions below 0.6 % [26, 15].

An ideal nanofluid for volumetric solar absorption must effectively absorb the solar radiation within the wavelength range 300 nm $< \lambda <$ 2500 nm. Taylor et al. [26] studied the best conditions for efficiently absorbing solar radiation in this wavelength range and convert into heat within the working fluid. The nanofluids prepared in the project were expected to absorb $>$ 95 % of the AM1.5 direct normal radiation with a fluid depth of 10 cm. Another significant result of this study proved that nanoparticles mainly absorb radiation in the shorter wavelengths of the solar spectrum, while the base fluid absorbs radiation with longer wavelengths in the infrared spectrum

(> 900 nm). Water actually proves to be a more efficient absorber of solar radiation than nanoparticles at these wavelengths. Therefore, water will emit most radiation at long wavelengths, behaving like a blackbody [26].

Struchalin et al. [37] measured the extinction coefficients corresponding to different concentrations of carbon black nanofluids for two wavelength ranges of the solar spectrum. The first range includes the wavelengths 400 - 1100 nm (1), and the second range corresponds to wavelengths 1000 - 1700 nm (2). The extinction coefficient values are plotted in figure 11. In the introduction, it was mentioned that the photovoltaic cell only converts solar energy into electrical energy at wavelengths between 700 and 1100 nm, and figure 8 shows that the intensity peaks between 400 and 700 nm. Therefore, it is sufficient to use the extinction coefficients from range (1) in the case of this project and consider it to be the average extinction coefficient over the entire range of incident solar radiation.

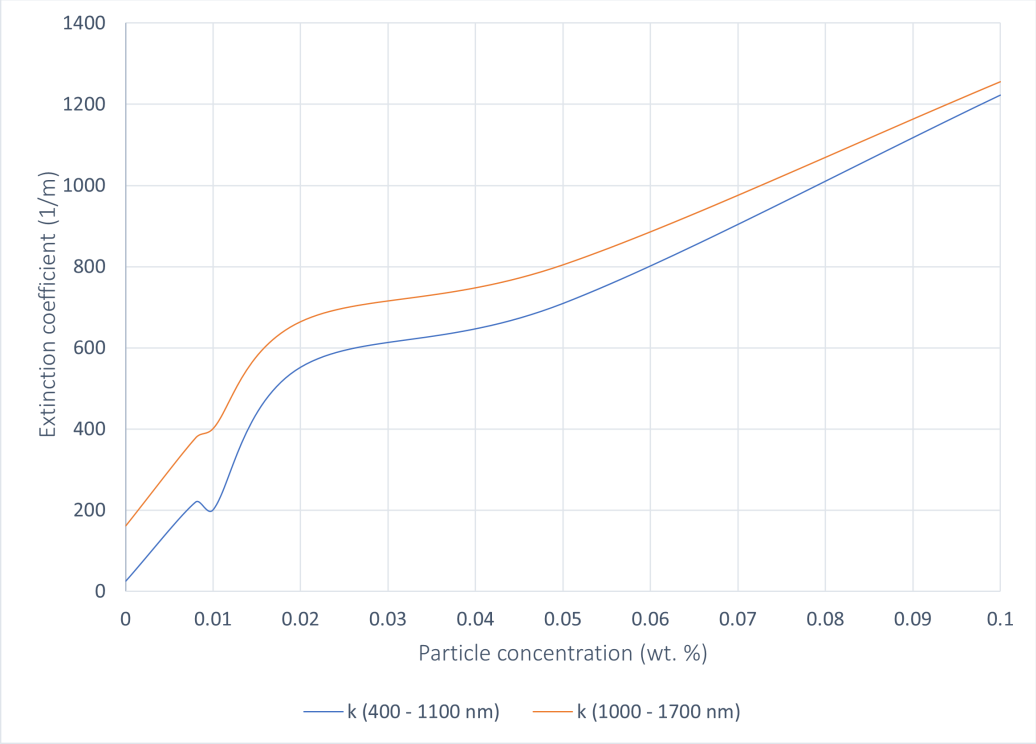

Figure 11: Measured extinction coefficient for different volume fractions. The data is obtained from Struchalin et al. [37]

2.3.2 Thermophysical properties

The thermophysical properties of a fluid are decisive in the fluid's thermal abilities. They include the specific heat capacity, thermal conductivity, viscosity, the heat transfer coefficient, density, and surface tension. To decide the thermal performance of a heat transfer fluid, it is necessary to look at how these thermophysical properties behave when the system's operating conditions are changed. Operating parameters for a nanofluid can be temperature, ambient conditions, base fluid, particle size, particle shape, and particle concentration. These parameters need to be chosen correctly to obtain the most efficient thermal properties [5].

Thermal conductivity

Thermal conductivity is a material's ability to conduct heat and is defined as the proportionality between heat flux and temperature gradient. The property is critical when considering the thermal performance of a heat transfer fluid. Dispersing nanoparticles into a base fluid is known to enhance the thermal conductivity significantly ([22], [59], [60], [61]). Several factors affect the thermal conductivity of a nanofluid, and the most important factors are the material, particle size, temperature, pH-value, Brownian particle motion, base fluid, specific surface area, particle concentration, and stability [5, 19]. Increasing the particle size will, in most cases, cause the nanofluid to become unstable, negatively affecting the thermal conductivity. Specific surface area is the ratio between the particle surface area and mass, and an increase of this parameter creates a larger surface for heat transfer from the particles, increasing the thermal conductivity. Increasing the temperature will increase thermal conductivity, and so will increasing the particle concentration. However, increasing the concentration too much will decrease the value because the nanofluid becomes unstable with agglomerates [19]. The material's thermal conductivity also affects the resulting nanofluid conductivity, in most cases positively because solids generally have higher thermal conductivity than fluids. Unstable nanofluids will quickly form agglomerates and decrease thermal conductivity. Therefore, stabilizing additives might be necessary. Brownian motion of the particles is the most crucial factor thermal conductivity depends on [24, 21]. This is the key mechanism that controls the thermal behavior of the fluid-particle suspension and is directly connected to the temperature of the fluid. Figure 12 is a schematic of the essential factors that affect the thermal conductivity of a nanofluid.

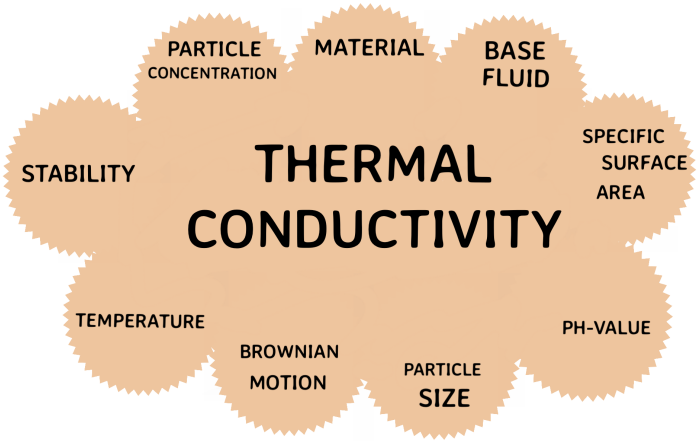

Figure 12: Schematic showing factors affecting the thermal conductivity of a nanofluid

From experiment, Lee et al. [23] concluded that thermal conductivity increases linearly with volume fraction for Al_2O_3 and water nanofluid. Masuda [61] studied the nanofluid's thermal conductivity by experiment. The highest enhancement of thermal conductivity in nanofluids to be reported was 32.4 % for Al_2O_3 nanofluid in temperature range 31.85 - 86.85 C. Chandrasekar et al. [59] measured the thermal conductivity of Al_2O_3 dispersed in water and achieved an enhancement of 9.7 % by increasing the particle concentration. Lee et al. [60] also found that suspending 4 % volume fraction of CuO particles in ethylene glycol resulted in a 20 % increase in thermal conductivity. Some researchers have observed an enhancement of thermal conductivity with increasing particle size, with volume concentrations of 1-2 %. Others have studied MWCNT and water nanofluids and concluded that they exhibit a higher thermal conductivity than other common nanofluids. It has also been concluded that base fluid type affects thermal conductivity. For instance, ethylene glycols have outperformed water for thermal conductivity matters in nanofluids [5].

2.3.3 Thermal and electrical efficiencies

There is a strong correlation between the temperature, solar irradiance, and electrical power conversion of photovoltaic panels [11, 12]. Decreasing solar radiation decreases electrical output, while an increasing cell temperature will decrease the electrical efficiency of the cell [12]. The equation for the electrical energy efficiency of the PV-panel is:

$$\eta_{PV} = \eta_{ref}(1 - \beta[T - T_{ref}]), \tag{19}$$

where η_{ref} is the reference efficiency of the photovoltaic panel, β is the temperature coefficient, T is the average temperature of the panel, and T_{ref} is the reference temperature of the panel [11].

In the case of a fluid film flow over the panel, the radiation attenuation from equation (18) in the fluid must be accounted for. Therefore the electrical efficiency of the panel becomes:

$$\eta_{PV,C} = \frac{I}{I_0}\eta_{PV} = \exp(-\sigma\delta)\eta_{PV}. \tag{20}$$

The thermal efficiency of a thin fluid film subject to heat transfer is:

$$\eta_{th} = \frac{\dot{m}c_p(T_{OUT} - T_{IN})}{q_0 A}, \tag{21}$$

where $\dot{m}$ is the mass flow rate, c_p is the specific heat of the fluid, and T_{IN} and T_{OUT} are the fluid temperatures at the inlet and outlet of the fluid flow, respectively [11].

Assuming that all the energy harvested in the fluid goes to heating, the total energy efficiency of the PV/T system is found by adding the right sides of equations (20) and (21):

$$\eta_{TOT} = \frac{\dot{m}c_p(T_{OUT} - T_{IN})}{q_0 A} + \exp(-\sigma\delta)\eta_{PV}. \tag{22}$$

2.4 Computational Fluid Dynamics

Computational fluid dynamics (CFD) is the process of finding a numerical solution to physical problems including fluid dynamics, using CFD software. Many physical processes are complicated and time-demanding to analyze through an experimental setup, and using CFD solves these problems. In such an analysis, the fluid flow is examined in accordance with its physical properties, simultaneously [62].

Three essential equations describe the relationship between the physical properties of interest for the analysis, which will be presented in this chapter. The mathematical models depend on the physical situation, for example, whether

it includes heat transfer, mass transfer, phase transfer, etc. It is also important to validate the model against theoretical or experimental analysis to achieve an accurate solution to the case [62]. In this project, the software used for the numerical analysis is Simsenter STAR-CCM+ 2020.1 from Siemens.

2.4.1 Governing Equations of CFD

All of the governing equations used in computational fluid dynamics are derived from the three laws of conservation, saying that mass, momentum, and energy are conserved within a closed system [62, 63]:

1. Conservation of mass - the continuity equation
2. Conservation of momentum - Newton's second law
3. Conservation of energy - the first law of thermodynamics

The physical flow variables velocity, pressure, and temperature must be obtained simultaneously from these three basic conservation equations. However, pressure and temperature are the two independent thermodynamic variables required. The final conservation equations also contain the thermodynamic values density ρ, enthalpy h, viscosity μ, and thermal conductivity k. These properties are decided from the independent values of pressure and temperature. For any physical case involving fluid flow, velocity, pressure, and temperature should be analyzed at every point in the flow [62].

A fluid flow regime can be investigated with a *Lagrangian* or a *Eulerian* approach. The principle of the Lagrangian method is calculating the properties of a volume element following the flow. This is a time-dependent method, where the computer follows the flow through space and time. The Eulerian method investigates the physical properties of the flow within a volume element fixed in space [62]. Figure 13 shows a volume element following the Lagrangian approach and another volume element that corresponds to an Eulerian approach.

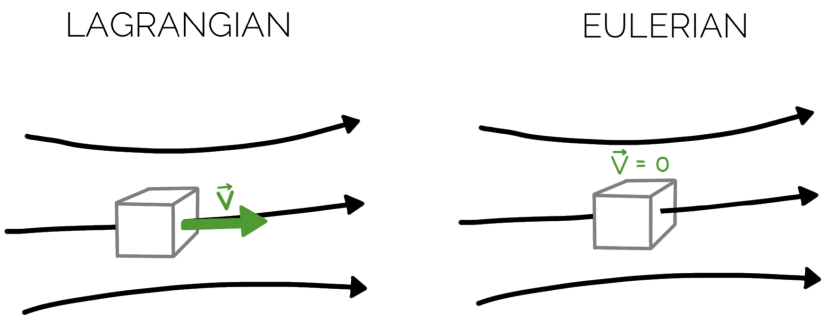

Figure 13: Volume element representation with a Lagrangian and an Eulerian approach

For a Lagrangian flow model, these equations describe the motion:

$$\begin{aligned} x &= x(a, b, c, t), \\ y &= y(a, b, c, t), \\ z &= z(a, b, c, t), \end{aligned} \tag{23}$$

where a, b, and c are the initial spatial coordinates of the volume element.

For an Eulerian flow model, it is the velocity components that are the unknown functions of the independent variables x, y, z, and t, giving the velocity components:

$$\begin{aligned} u &= u(x, y, z, t), \\ v &= v(x, y, z, t), \\ w &= w(x, y, z, t). \end{aligned} \tag{24}$$

Mass conservation

The mass conservation principle can be mathematically described as

$$\frac{D\rho}{Dt} + \rho(\nabla \cdot \mathbf{v}) = 0, \tag{25}$$

where $\frac{D}{Dt}$ is the substantial time derivative operator, $\mathbf{v}$ is the velocity, ρ is the density, and ∇ is the gradient operator. For incompressible flow, equation (25) becomes:

$$\frac{\partial u}{\partial x} + \frac{\partial v}{\partial y} + \frac{\partial w}{\partial z} = 0, \tag{26}$$

where u, v and w are the spatial velocity components in directions x, y and z, respectively. This equation is often referred to as the continuity equation [62].

Momentum Conservation

The equation for conservation of momentum, also referred to as the Navier-Stokes Equation, is:

$$\frac{D(\rho\mathbf{v})}{Dt} = -\nabla p + \nabla \cdot \mathbf{T} + \rho\mathbf{g}, \tag{27}$$

where ρ is the density, $\mathbf{T}$ is the viscous stress tensor, and $\rho\mathbf{g}$ is the gravitational force per unit volume [62].

The terms of the equation denote the local change of momentum with time, momentum convection, the surface force, the diffusion term, and the mass force, respectively.

For viscous, newtonian fluids, equation (27) simplifies to:

$$\frac{D(\rho\mathbf{v})}{Dt} = -\nabla p + \mu\nabla^2\mathbf{v} + \rho\mathbf{g} + \mathbf{F}, \tag{28}$$

where $\mathbf{F}$ represents any external forces on the fluid.

Energy Conservation

The equation for energy conservation is the third law of thermodynamics, and it states that the sum of the work and heat added to a system equals the increase in the system's internal energy.

$$dE = dQ + dW. \tag{29}$$

The energy equation is given as:

$$\frac{D(\rho(e+0.5|\mathbf{v}|^2)}{Dt} = -p\nabla\mathbf{v} + \rho\mathbf{v}\cdot\mathbf{g} + \nabla\cdot(\mathbf{T}\cdot\mathbf{v}) + q_v + \nabla\cdot(k\nabla T). \quad (30)$$

The first term of equation (30) denotes the rate of change of the total energy of the fluid with time where ρ is the density, e is the enthalpy, and $\mathbf{v}$ is the velocity. The second and third term make up the net work done by pressure and gravity, where p is the pressure. The next term is the viscous term where $\mathbf{T}$ is the viscous stress tensor, which physically is associated with the work done by shear stresses in the fluid. q_v is the volumetric heat due to radiation. Finally, the last term is the net heat to the fluid due to conductive heat transfer, where k is the thermal conductivity [63].

Mesh Independence Study

The CFD program separates the domain into many small subdomains, called cells, to get an accurate solution to the physical problem. All of the cells in the domain form the mesh. In other words, the domain of interest is discretized into these small cells to which the mathematical equations can be applied, assuming they have a linear behaviour within each cell. Therefore, in an area where a parameter is highly sensitive, the mesh needs to be finer. The mesh is a common cause of errors in the computed solution. When the mesh is not fine enough in the areas of highly fluctuating parameters, there is a high risk of getting results far from reality. To find the most suitable mesh for the physical problem, it is necessary to carry out a *mesh independence study*. Properties like cell type, cell number, and computation time are essential to obtain an accurate solution. This mesh optimizing method depends on the conditions of the physical problem, but for a thin fluid film over a flat plate, the steps can be:

1. Prism layer total thickness independence
2. Number of prism layers independence
3. Base size independence

Convergence

In computational fluid dynamics, convergence is an important issue. The convergence of a solution is affected by factors like phase change, turbulence, and mass transfer. The convergence is controlled by the error between the solutions of the last two stages of computation, meaning how much the solution fluctuates between the stages. The less this error is, the more stable,

hence more accurate the solution is. Even though the solution converges, it does not always mean it is correct. To achieve convergence, the mesh can be refined or changed in other ways. It is also important to repeat the solution to avoid ambiguities in the simulating process [62].

Laminar and Turbulent Flow

Laminar and turbulent flow patterns differ a lot, generating very different solutions in computer software. A turbulent flow case takes much more computing power than a laminar flow case. This is because a turbulent flow is not steady, so it will change over time, requiring the entire domain to be recalculated for each time step [62].

Thin Fluid Film Model

For simulation of a running fluid film, STAR-CCM+ can offer several possible solutions to solve the problem. The *Thin Fluid Film* model takes into consideration the complex interactions between the film, the surroundings, and the surface over which the film flows. There are for this model many options on how to model the film. It is possible to define an initial film layer on the surface, boundary surfaces can be defined as fluid film inlets and outlets, fluid film mass sinks and sources can be defined, and a phase changing gas can be defined in a region and evaporate to create a fluid film. The model solves the transport equations for mass, momentum, energy, species, and volume fraction [64]. In the model, a shell region is created within the initial domain created as a one-cell thick two-dimensional surface domain. The boundaries for the domain are edges and interfaces to the surface and surroundings. The model assumes that the fluid film is created on one of the bounding surfaces of a background fluid region, for example, air. The velocity profile is assumed to be parabolic in the model, as shown in figure 6. The model also assumes the layer to be thin enough for the flow to be laminar by the laminar boundary layer approximation [64].

A physics continuum in a region must be specified before setting up a fluid film on a region. The solvers of the model are:

- Fluid film segregated flow solver,
- Film velocity solver (momentum conservation),
- Film thickness solver (mass conservation).

Mass conservation in the model is solved by using equation (26) and can be applied to several species of a multicomponent film to calculate the film

thickness. Momentum conservation is solved for equation (28), where the momentum source term **F** in the equation is due to the capillary force. Lastly, the energy equation is solved by using equation (30). When the fluid film volume fraction is solved, the film occupied volume is subtracted from the gas phase volume in the cells adjacent to the fluid film.

3 Methods

3.1 Computational Fluid Dynamics Model

3.1.1 Model description

Figure 14 shows the entire PV/T setup of the study. The model consists of an inclined solar cell at the bottom (3), covered by a flat plate direct absorption solar collector (DASC) with a fluid film flowing over the panel (2) with a fluid inlet (1). Figure 15 displays a schematic of the model's dimensions. Assumptions made for the system are:

- Steady temperature distribution,
- Newtonian fluid,
- Laminar flow,
- Steady flow,
- No slip at the solid surface.

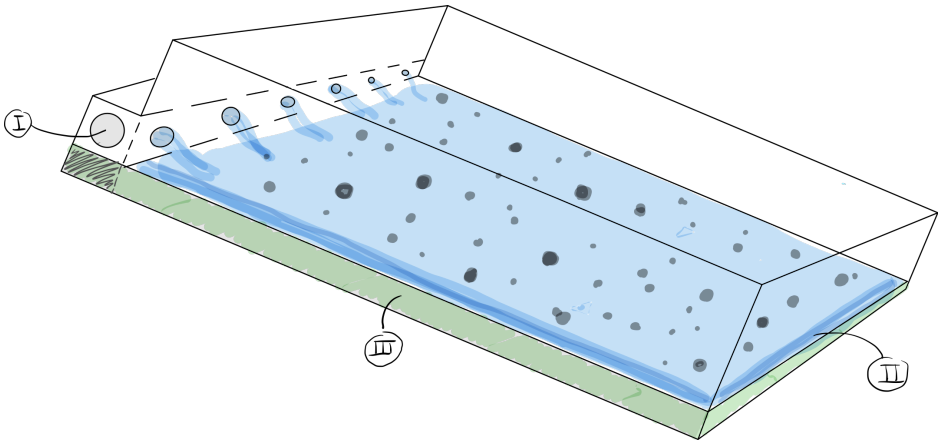

Figure 14: Sketch of the PV/T

Dimensions	1610 x 950 x 38 mm
Weight	18 kg
Temperature coefficient β	-0.4 %/°C
Reference efficiency η_{REF}	15.8 %
Reference temperature $\mathbf{T}_{REF}$	25 °C
Reference irradiation $\mathbf{I}_{REF}$	1000 W/m^2

Table 1: Specifications for the photovoltaic panel, obtained from [65]

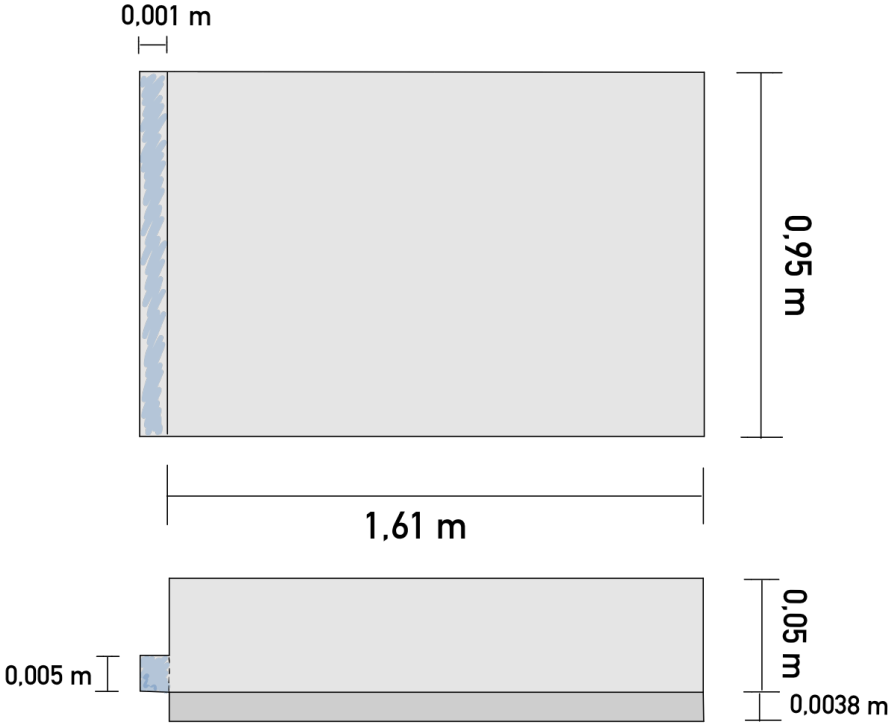

Figure 15: Dimensions of the PV/T system

Table 1 contains all the properties of the photovoltaic panel necessary for the numerical calculations obtained from REC Group [65].

Because the fluid flow is assumed to be symmetric in the direction parallel with the inlet step, the geometry in STAR-CCM+ is simplified by shortening this side. This is to give the simulated model a more competitive computational running time, which is always a goal when running computer simulations. The model used for the simulating process in STAR-CCM+ is the *Thin fluid film model*, which is described in detail in Chapter 2.4.1.

The other physical models chosen in the simulation correspond to the case of constant density of the media, laminar flow, and segregated flow and fluid temperature. The *implicit unsteady* model is also added, which only means that an iterative procedure to find the value of a quantity at a given time-step in the simulation is used. In practice this means that the solution at each point in the domain is updated for each time step, thus the solution is dependent on time. The background domain in the model is chosen to be air.

3.1.2 Creating the Mesh

To have a competitive running time for the simulation and achieve the most accurate results, a mesh independence study was carried out. The aim was to study which type of mesh gives the most accurate results compared to the theoretical value for the fluid film thickness. The mesh independence study was carried out by varying the base size, the number of prism layers, and prism layer total thickness, one at a time. The simulated fluid film thickness was compared to the theoretically calculated value from equation (5). The mass flow rate is kept at 5 kg/min during the entire mesh independence study.

Prism layer total thickness independence

In the first case, the base size was set to 0.015 m, while the number of prism layers was set to 2. The error between the theoretically and numerically calculated film thickness versus the prism layer total thickness is plotted in figure 16, and the exact values are shown in table 7 in Appendix A.

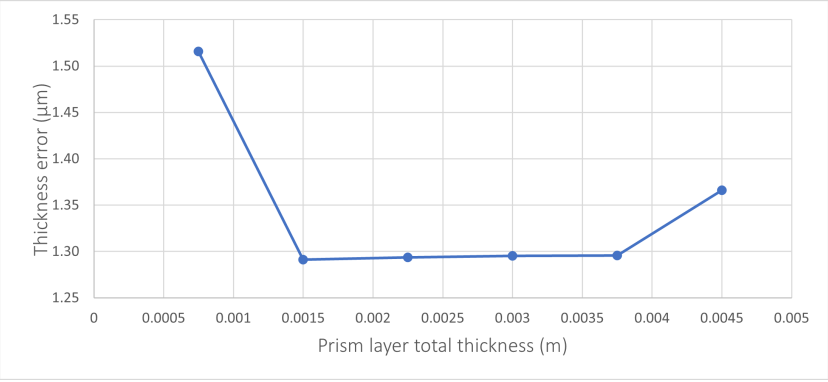

Figure 16: Fluid film thickness error vs prism layer total thickness

The optimal value for the prism layer total thickness is 0.0015 m in this case, which is 10% of the base size.

Number of prism layers independence

When deciding the number of prism layers, the base size was kept at 0.015 m and the prism layer total thickness was 0.0015 m as shown above. The film thickness error value is shown for a varying number of prism layers in figure 17. The values are displayed in table 8 in Appendix A.

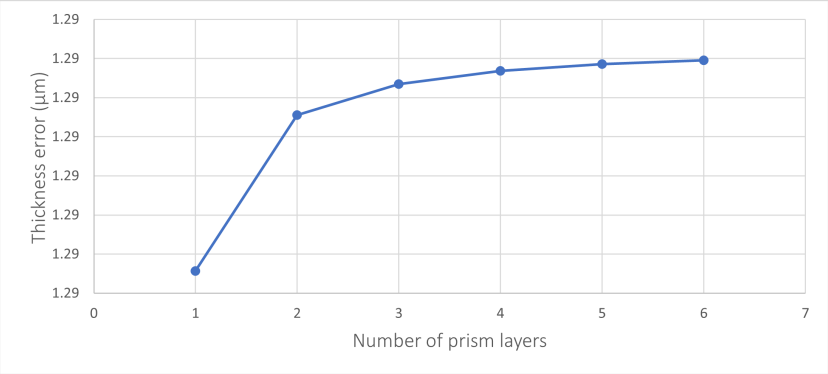

Figure 17: Fluid film thickness error vs number of prism layers

According to the simulated results, the lowest error is achieved when the number of prism layers is 1. However, the error value seems to converge for 6 prism layers, and a more accurate solution is therefore likely.

Base size independence

The obtained values for the number of prism layers and the prism layer total thickness are used when finding the optimal base size. The film thickness error is plotted versus base size values in figure 18. The plotted values can also be seen in table 9 in Appendix A.

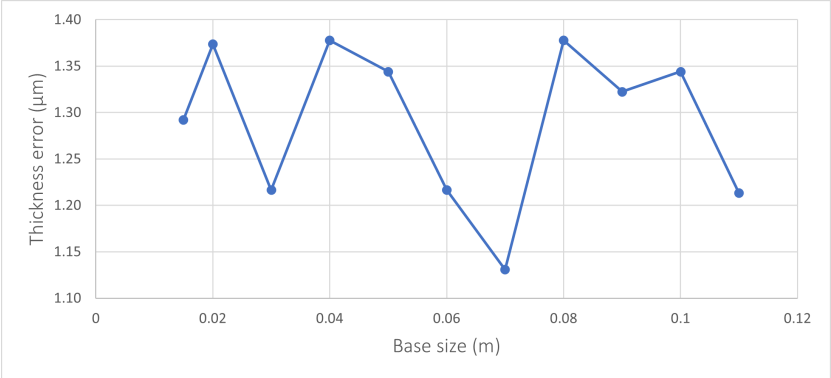

Figure 18: Fluid film thickness error vs base size

Because of the alternating values of thickness error in the figure, the simulation was run for base sizes outside this range as well. It was observed that the alternating behaviour repeats itself. The lowest film thickness error is found when the base size is equal to multiples of 0.07 m. Considering these results, the base size was set to 0.07 m. The optimized mesh parameters are presented in table 2.

Prism layer total thickness (m)	**Number of prism layers**	**Base size (m)**
0.0015	6	0.07

Table 2: Optimal values for the mesh

After implementing these values in the simulation, the resulting error between the theoretical and numerical solution for fluid film thickness is 1.1 μm, which is $\approx$ 3.5 % of the theoretically calculated fluid film thickness. An image of the mesh is shown in figure 19.

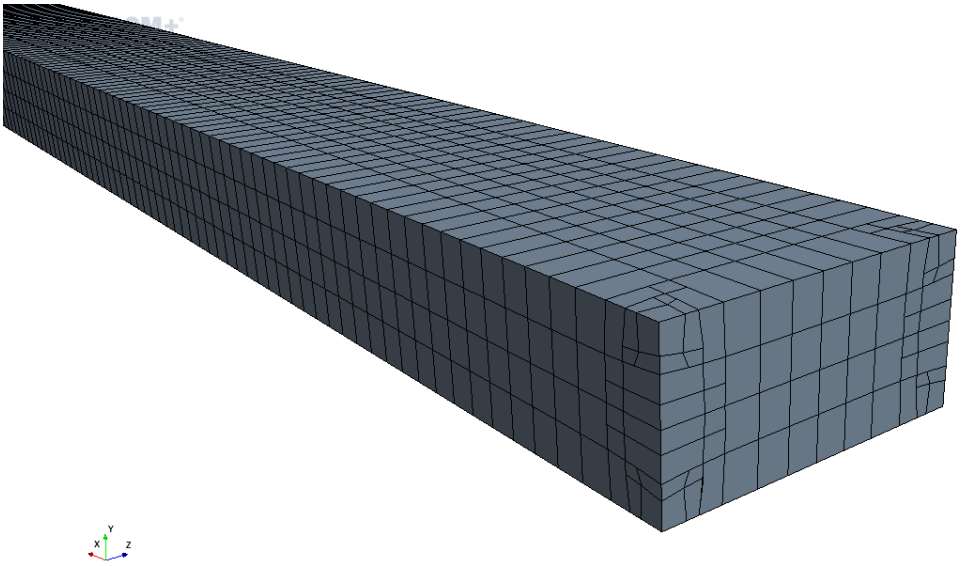

Figure 19: Mesh image in STAR-CCM+

3.1.3 Model Validation

The use of computational fluid dynamics as a tool for predicting the behaviour of physical flow systems is widespread. Therefore, it is relevant to question the accuracy of the solutions this method yields [66]. A validation study of the model is therefore crucial for deciding the reliability of the model. The simulated values for outlet temperature and fluid film thickness were compared to theoretical models. The model validation was carried out with no present radiation or other external heat sources. The parameters set for the fluid are associated with water.

Figure 20, obtained from [53], is an experimentally developed figure showing the temperature distribution in the laminar boundary layer in flat plate flow. This figure was chosen to validate the simulation results.

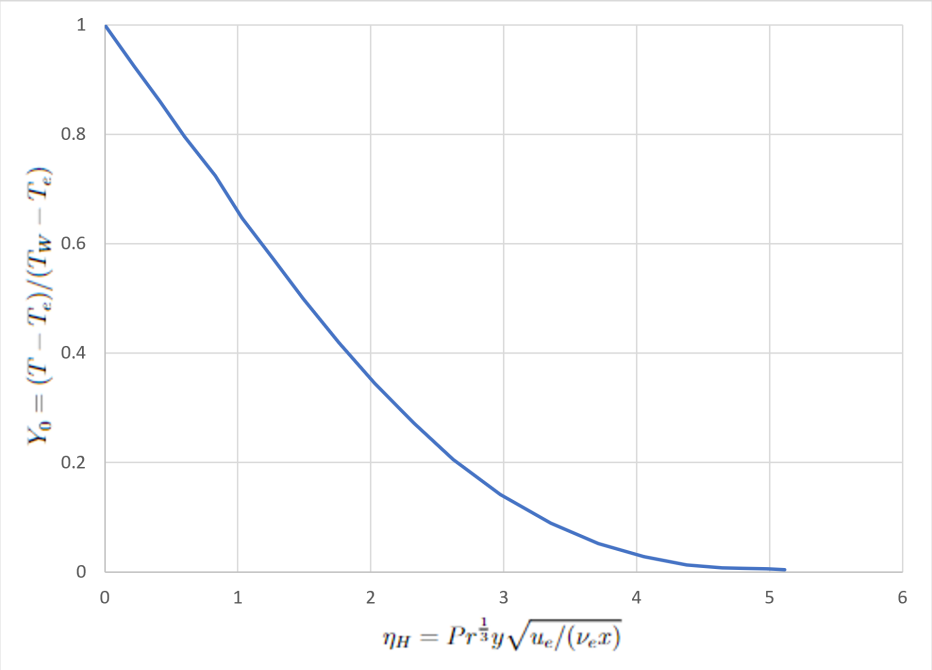

Figure 20: Theoretical model for temperature distribution in the laminar boundary layer of flat plate flow. The figure is reproduced from [53]

In the model, y denotes half the fluid film thickness, and the velocity at this position is considered to be the average fluid velocity. The parameter x is the spatial coordinate along the plate, which in this case was set equal to the length of the panel because the temperature was to be studied at the fluid flow outlet. ν_e, u_e, and T_e are the kinematic viscosity, the x-component of the velocity, and the fluid temperature considered at the leading edge, respectively. Furthermore, T_w is the average wall temperature, and T is the fluid temperature at the outlet. To compare several results from the theoretical model with the simulation, the wall temperature was varied from 10 to 60 °C. The mass flow rate was held at 5 kg/s. The surface average temperature at the fluid outlet was studied in the simulation. When the simulation converged, the resulting values were compared with the theoretical values calculated from the model in figure 20.

In addition, the numerically solved values for fluid film thickness was validated against the theoretical formula in equation (5). The film thickness was solved at mass flow rates from 1 to 10 kg/min, and the plate temperature was held at a constant value of 20 °C. The error between the theoretical and numerical results were found and discussed for all the flow rates.

3.1.4 Thermal Balance

It is essential to obtain thermal balance for the PV panel to complete a numerical analysis of the model. This is done by applying the first law of thermodynamics, where the internal energy change is

$$\frac{\partial U}{\partial t} = q_{in} - q_{out} + q_g, \tag{31}$$

where q_{in} is the heat transfer rate into a system, q_{out} is the heat transfer rate out of a system, and q_q is the heat generation rate in the system [13].

From equation (16) describing the thermal radiation emission from an engineering surface to another body, the radiative heat loss to the surroundings from the photovoltaic panel can be expressed as:

$$q = \sigma \epsilon A (T_{PV}^4 – T_{AMB}^4). \tag{32}$$

Here, T_{PV} is the uniform temperature of the panel, while T_{AMB} is the ambient temperature.

The convective heat transfer from the bottom of the panel to the surroundings due to temperature gradient is derived from *Newton's law of cooling* given in equation (8) and is expressed as:

$$q = hA(T_{PV} - T_{AMB}), \tag{33}$$

where h is the heat transfer coefficient. The amount of heat transfer to the fluid is expressed as:

$$q = \dot{m} c_{p,F} (T_{OUT} - T_{IN}), \tag{34}$$

where in this case, T_{IN} is the inlet fluid temperature, T_{OUT} is the outlet fluid temperature and $\dot{m}$ is the mass flow rate of the fluid.

The transient condition for the total amount of heat in the panel is given as:

$$q = m_{PV} c_{p,PV} \frac{dT_{PV}}{dt}, \tag{35}$$

where m_{PV} is the mass of the PV-panel, c_{PV} is the specific heat of the panel, and T_{PV} is the temperature of the panel [53].

Lambert-Beer's law expresses the solar radiation transmitted through the fluid film in equation (18), where the heat is:

$$q = q_0 e^{-\sigma\delta} A. \tag{36}$$

Some radiation transmitted to the panel will be transformed into electrical energy within the panel, and this energy is derived from the equation (19) for electrical efficiency, giving:

$$q = \eta_{PV} q_0 e^{-\sigma\delta} A, \tag{37}$$

where A is the area of the top surface of the panel [18]. Now, applying equations (32) - (37) to equation (31), the thermal balance equation for the panel is obtained as:

$$\begin{aligned} m_{PV} c_{p,PV} \frac{dT_{PV}}{dt} &= q_0 e^{-\sigma\delta} A - \dot{m} c_{p,F} (T_{OUT} - T_{IN}) \\ -hA(T_{PV} - T_{AMB}) - \sigma\epsilon A(T_{PV}^4 - T_{AMB}^4) &- \eta_{PV} q_0 e^{-\sigma\delta} A. \end{aligned} \tag{38}$$

The thermal balance equation (31) was implemented in the simulation as a field function and set as boundary heat flux on the solar panel surface, which is the wall upon which the film flows. Beer-Lambert's law from equation (18) was implemented as "Energy Source Option" to the fluid film region. The values for the extinction coefficients from figure 11 were used in the simulating process, which is assumed constant for radiation from 400 - 1100 nm. As mentioned earlier, this is the most energetic range of the solar radiation spectrum and contains the bandgap wavelengths of the photovoltaic panel. Because of this simplification, the absorption coefficient of the fluid is assumed to be constant over the entire solar radiation spectrum.

Monitored values

The monitored values were surface average temperature at the outlet and the photovoltaic panel surface, and field functions with the electrical and thermal efficiencies in equations (20) and (21) were also reported. First, the case without cooling or absorption was run. Then, the simulation was run

Parameter	Value
Film thickness at inlet	5 mm
Fluid temperature at inlet	20 °C
Initial PV surface temperature	20 °C
Constant ambient temperature	20 °C
Radiation Heat Flux	1000 W/m^2

Table 3: Conditions for the Model in STAR-CCM+

for extinction coefficient values 50 - 1000 m^{-1} for the mass flow rates of 1, 5, and 10 kg/min.

The system's boundary conditions, initial conditions, and static conditions are shown in table 3.

3.2 Thermal Conductivity Experiment

3.2.1 Motivation

To better understand the effect of dispersing nanoparticles into a base fluid, it is necessary to carry out experimental measurements of thermophysical properties. Thermal conductivity, dynamic viscosity, surface tension, density, and specific heat are interesting properties to understanding the heat transfer performance of fluid [22].

As mentioned in Chapter 2.3.2, many researchers have reported an increased thermal conductivity when increasing the nanoparticle concentration in a nanofluid for different nanoparticle materials. However, many experiments are only carried out for low particle concentrations (< 1 wt.%). In addition to optical filtering, the PV/T system of this study holds potential for thermal cooling as well. This would be implemented so that the temperature of the photovoltaic panel controls the fluid flow. This way, the solar cell will be exposed to all solar radiation during a specific period to be cooled by a high concentration nanofluid. As mentioned earlier, very low particle concentrations rarely result in any significant enhancement to heat transfer properties of a fluid, but this is not the case for higher concentrations. Therefore, this part of the study aims to gain an understanding of how a high concentration of carbon black particles dispersed in a base fluid affects the fluid thermal conductivity.

In this part of the project, carbon black nanofluids were prepared at concentrations 0.5 wt.% - 6 wt.%, and different base fluids were used. This was done due to challenges with instability and to see how the base fluid affects the results. The thermal conductivity of the freshly prepared nanofluids was measured with a laboratory thermal measuring device.

3.2.2 Nanofluid Preparation

The nanoparticle types used in this experiment are carbon nanofibres from Bergen Carbon Solutions [67] and carbon black spherical nanoparticles from Timcal Ensaco [68].

Bergen Carbon Solutions use advanced and innovative nanotechnology to transform CO_2 into carbon and oxygen. This production method is, therefore, also a contributor to reducing the CO_2 emissions [67]. The length of the nanofibres is > 5 μm, and the thickness is > 50 nm. The manufactured properties of the nanofibers are given in table 4.

Property	Value	Unit
Carbon content	< 95	%
CNF content	> 80	%
Length	> 5	μm
Thickness	> 50	nm
Metal impurities	≤ 10	%

Table 4: Manufactured properties of carbon nanofibers

The base fluids in this experiment were water-based with applied sodium dodecyl sulfate (SDS) and Triton X-100, individually.

SDS is an anionic (negatively ionized) surfactant often used as a stabilizing surfactant in nanofluids [69]. Several nanofluid research projects have achieved good stability results when applying 1 wt.% SDS in the nanofluid, some of them are Taylor et al. [26] and Struchalin et al. [37]. Sedong et al. [45] did an experimental study and reported that using SDS as a surfactant for carbon-based nanofluids would yield higher stability than using other surfactants. This also implies that higher thermal conductivity is achieved, which, as mentioned, is desirable for a heat transfer fluid.

Triton X-100 is a non-ionic dispersant that differs from surfactants such as SDS on a molecular level [69]. The surfactant is often applied to bring down the surface tension of a media [70]. Several researchers have reported high stability and heat transfer enhancement by using Triton X-100 ([22], [69], [71], [70]). Assael et al. [69] did an experimental study on the thermal conductivity of MWCNT nanofluids with different surfactants (for instance SDS and Triton X-100). They achieved enhancement values up to 13 % when using Triton X-100, but concluded that the other ionic surfactants were favourable for enhancement increase of MWCNT nanofluids. For TiO_2-deionized water nanofluid, Sözen et al. [70] reported that Triton X-100 was the most effective surfactant compared to the ionic surfactant Sodium Dodecyl Benzene Sulfonate (SDBS).

The correct weight of nanoparticles and base fluid was measured with a Mettler Toledo weight scale [72], with an uncertainty of 0.001 g. The nanofluids were dispersed by an ultrasonic probe (UP200Ht [73]), with sonication duration of 40, 60, and 120 minutes. The powers applied were 50 W and 200 W. This device was also used for the sonication process by Taylor et al. [26] and Hamze [22], and was as mentioned reported to work better than a bath sonicator to break up agglomerates.

3.2.3 Thermal Conductivity Measurements

The transient hot-wire (THW) method was applied for the thermal conductivity measurement part of the experiment. This method is often stated to be the quickest and most accurate way to measure the thermal conductivity of a fluid ([22], [74]). The method is extensively used in literature ([75], [45]). The device THW-L2 (Thermtest Inc., Canada) was used for the measurements, with an uncertainty of 5 % [22]. The device consists of a thin alumel wire (60 mm long and 0.1 mm thick), which is heated during the measuring. Figure 21 contains a detailed sketch of the fluid container and the part of the measuring device in contact with the fluid. The wire is fully inserted into the fluid. The fluid container only requires about 20 ml for a measurement.

First, the fluid was poured into the container. It was further placed into a heat bath. Once the desired temperature (20 °C) was achieved, the measurement was initialized manually in Thermtest, which is the computer software corresponding to the device. All of the individual parts of the measuring system are illustrated in figure 22. Each sample was measured five times, with at least 5 minutes between each measurement. The average value was calculated as the resulting thermal conductivity. Hamze et al. [22] achieved good results with this device in their study compared to theory and other studies.

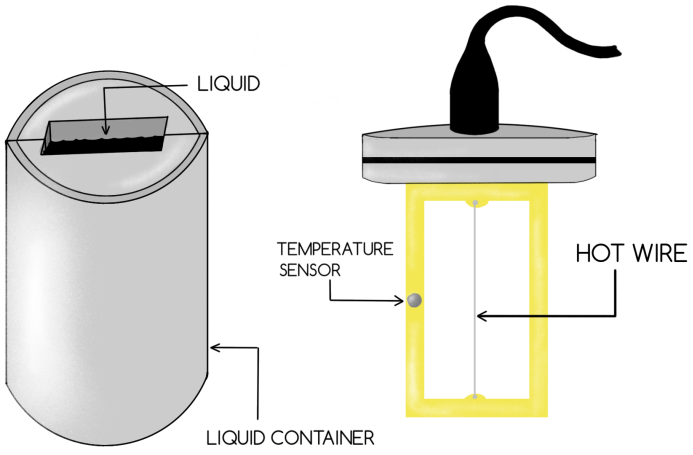

Figure 21: Sketch of the container with liquid and the part of the measuring device in contact with it

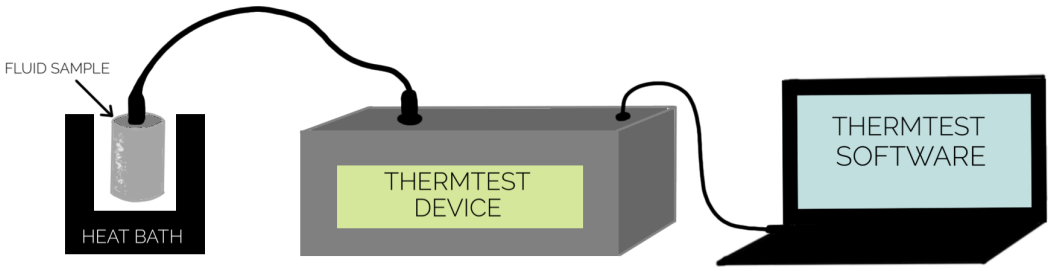

Figure 22: Sketch of all the connected parts of the experimental setup

Distilled water was used for the base fluids in all cases. Before performing measurements on the nanofluids, the device was calibrated with distilled water. Measurements were performed for base fluids where there were no nanoparticles dispersed. Nanofluids of concentrations 0.5, 2, 4, and 6 wt.% were prepared and measured. Due to problems with achieving stable nanofluids and limited time in the laboratory, the results differed significantly. Unfortunately, there was no time to prepare and measure all the concentrations with the same preparation method and base fluid. The measurement results are gathered in tables 13 - 16 in Appendix B.

For a small dataset of N measurements (usually 5 to 10) where the uncertainties differ for each measurement, the uncertainty of the average value is:

$$\Delta x_{avg} = \frac{\sqrt{(\Delta x_1)^2 + (\Delta x_2)^2 + (\Delta x_3)^2 + ...}}{N}. \tag{39}$$

Equation (39) from [76] was used to calculate the uncertainties of all the mean values of measured thermal conductivity. For calculating the uncertainty of the addition $z = x + y$, the uncertainty can be calculated like this:

$$\Delta z = \sqrt{(\Delta x)^2 + (\Delta y)^2}, \tag{40}$$

and for the division part $z = \frac{x}{y}$, the calculated uncertainty is:

$$\Delta z = |\frac{x}{y}|\sqrt{\left(\frac{\Delta x}{x}\right)^2 + \left(\frac{\Delta y}{y}\right)^2}. \tag{41}$$

For calculating the uncertainties for mass concentrations of surfactant and particle concentration, equations (40) and (41) were combined.

4 Results and Discussion

4.1 Computational Fluid Dynamics Results

4.1.1 Model Validation

Figure 23 displays the numerically and theoretically solved fluid outlet temperatures, together with the corresponding static flat plane temperature. Table 6 in Appendix A.1 shows the results in a plot.

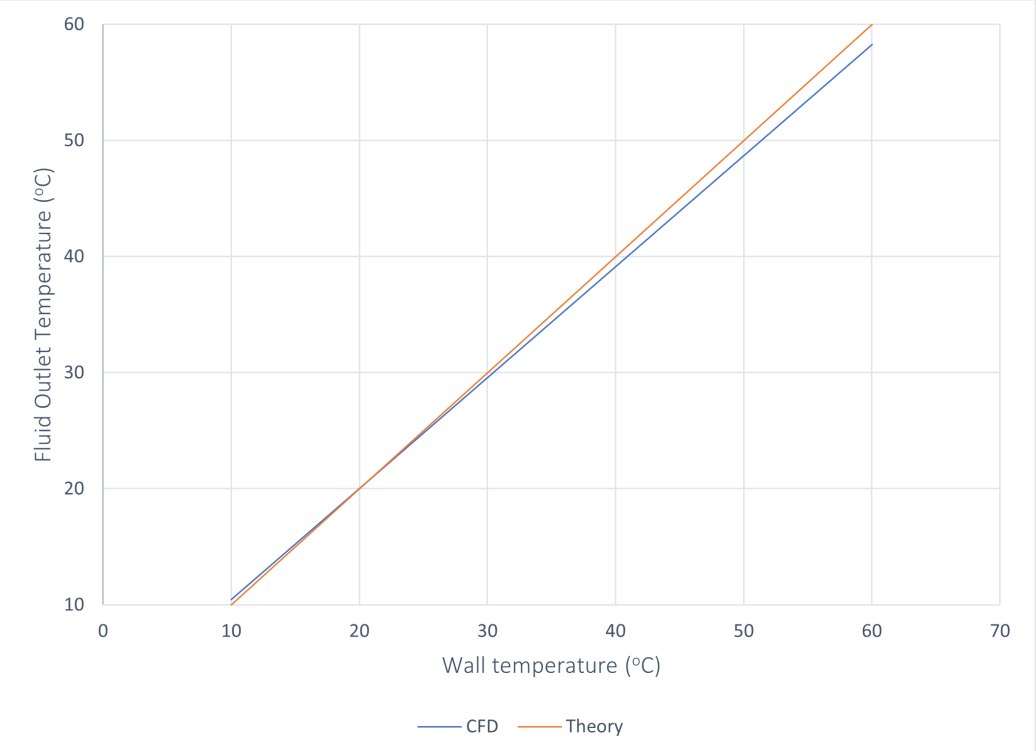

Figure 23: Theoretically and numerically solved fluid outlet temperature (vertical axis) vs static wall temperature (horizontal axis)

It can be seen from the figure that the results agree very well within the chosen temperature range. The error between the theory and simulation seems to increase with increasing wall temperature. This is likely because the CFD model captures the heat loss to the surroundings, which was not considered in the theoretical model with results depicted in figure 20. The highest error between the values is 3 % of the theoretical value for a plate temperature of 60 °C. Higher temperature leads to higher heat loss; therefore, the error will probably continue to increase with increasing temperature. However, in the chosen range of temperatures, the model is successfully validated by the theory.

The theoretically and numerically solved values of the fluid film thickness for different mass flow rates between 1 and 10 kg/min are displayed in figure 24. It can be seen that the compared values lie very close to one another; in fact, the highest error found is only 2 % of the theoretical value for a mass flow rate of 1 kg/min.

These two validation methods yield high accuracy for the model in STAR-CCM+. It is safe to say that the model is a good representation of the theory. However, it is difficult to tell how these results would compare to an experimental study of this same system. To further validate the model, an analogous comparison might be helpful. As indicated above, it is important to note that there were no external heat sources to the fluid or plate in the model validation process.

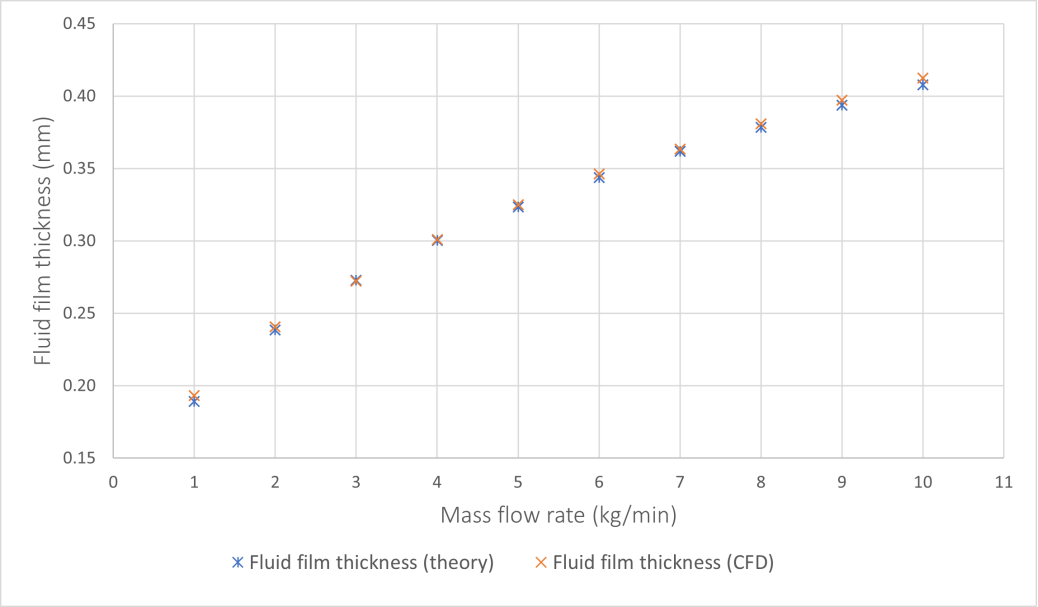

Figure 24: Comparison plot between theoretical and numerically solved fluid film thickness

Figure 25 displays the temperature distribution of the fluid film along the panel, while figure 26 shows the fluid film thickness while the fluid moves down the panel. The image shows the fluid film when it has only covered about half of the length of the plane, hence it has not yet reached a steady state. As can be seen in the figure, the fluid film thickness beyond this point is equal to 0 m.

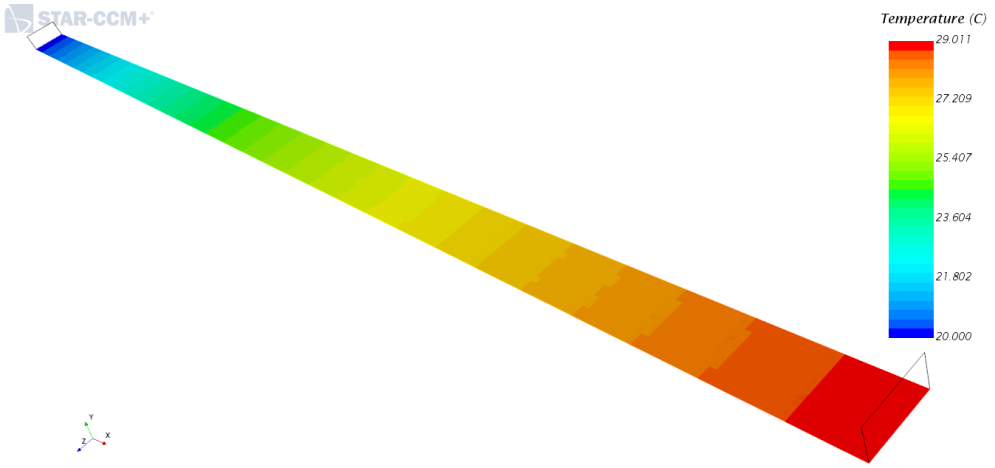

Figure 25: Temperature distribution of the fluid film (the extinction coefficient is set to 800 m^{-1} and the mass flow rate is 1 kg/min)

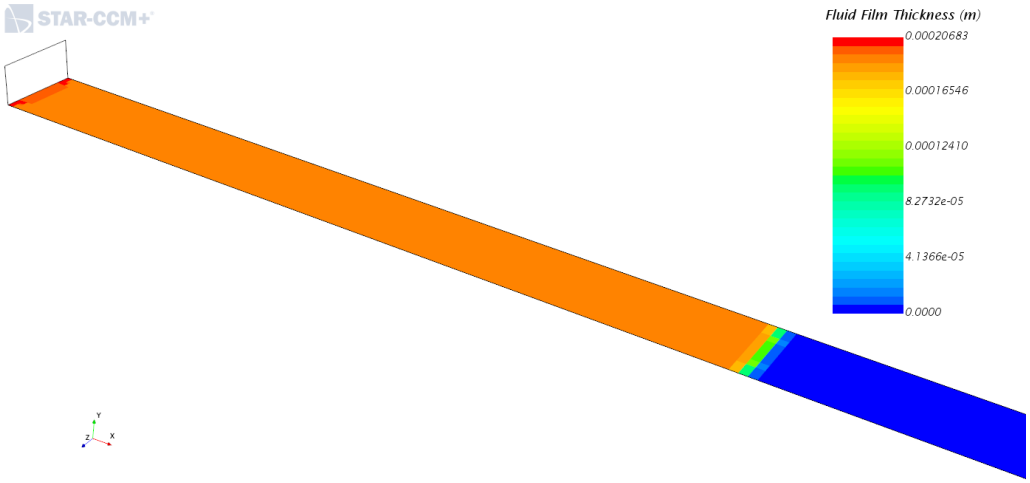

Figure 26: Fluid film thickness of the fluid film moving down the panel

Figure 27 shows the fluid film thickness plot in STAR-CCM+. In this case the extinction coefficient is set to 800 m^{-1} and the mass flow rate is 1 kg/min. It can be seen that the fluid film thickness is ≈ 0.19 mm for this case.

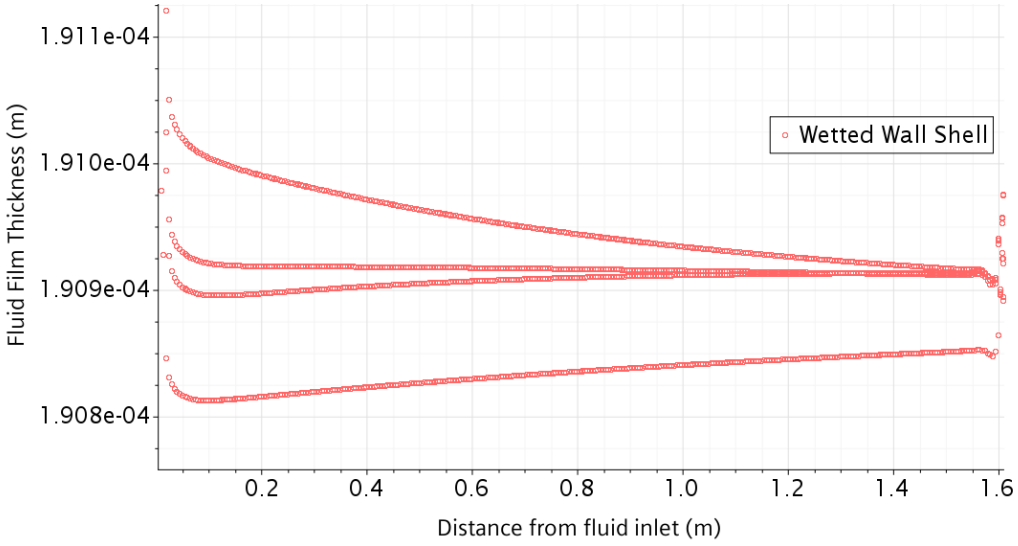

Figure 27: Plot showing the fluid film thickness in the steady flow (the extinction coefficient is set to 800 m^{-1} and the mass flow rate is 1 kg/min)

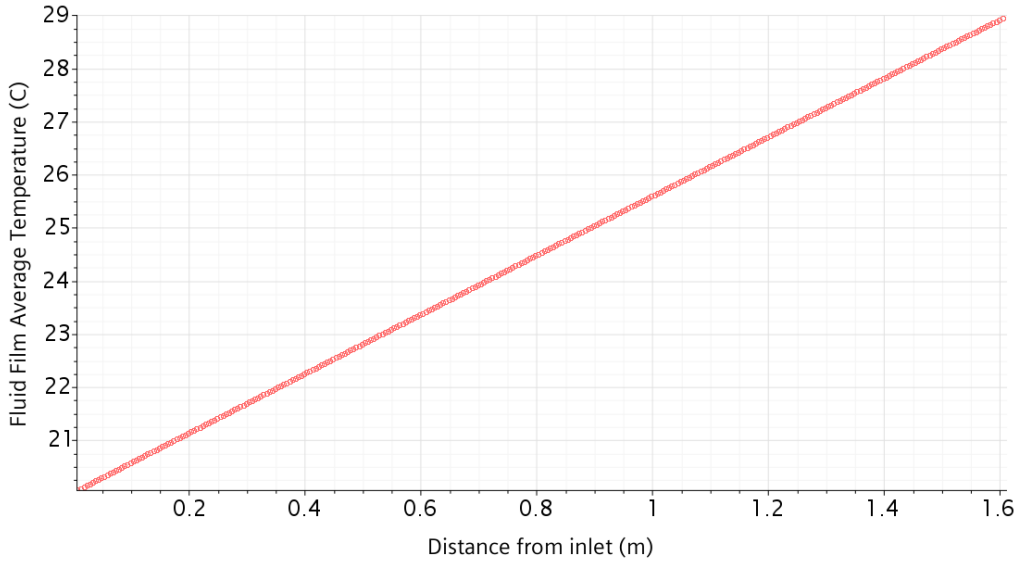

Figure 28: Plot showing the fluid film average temperature in the steady flow (the extinction coefficient is set to 800 m^{-1} and the mass flow rate is 1 kg/min)

4.1.2 Efficiency of the System

The numerically solved photovoltaic panel temperature and electrical efficiency without a fluid film on top are shown in table 5. As it can be seen, the resulting electrical efficiency is 11.6 %. In an experimental study, Al-Shohani et al. [77] observed a Si-cell electrical efficiency of 12.1 %, which is close to this value.

Intensity (W/m^2)	T_{PV} (°C)	$\eta_{electrical}$ (%)
1000	91.4	11.6

Table 5: Simulated case of PV efficiency without cooling

The plots in figures 29, 30 and 31 display the simulated electrical, thermal and total efficiencies for mass flow rates 1 kg/min, 5 kg/min and 10 kg/min, respectively. Tables 10, 11 and 12 in Appendix A show data from the same results.

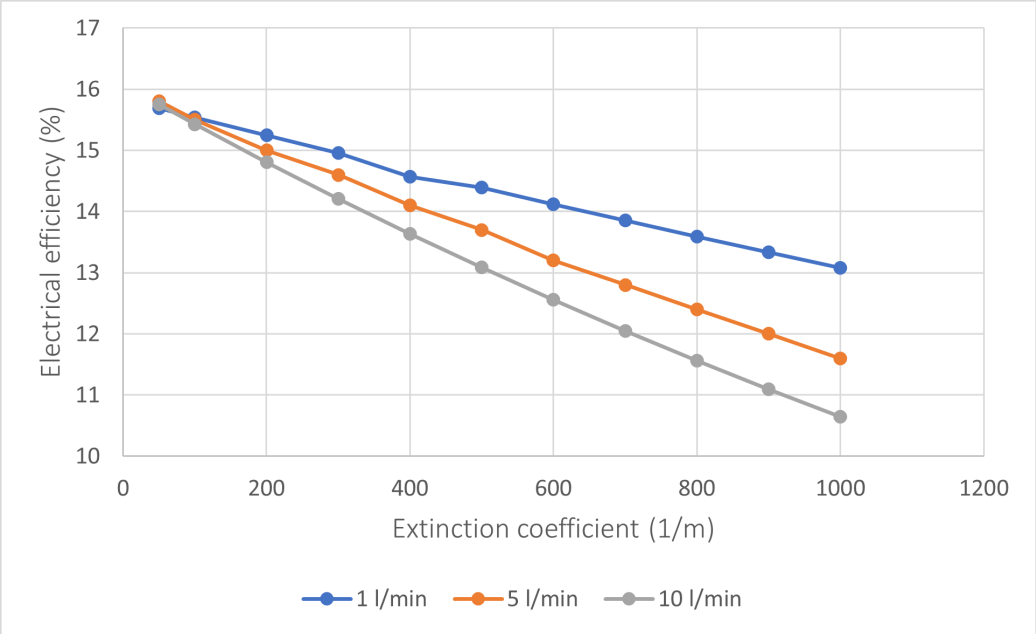

Figure 29: The electrical efficiency obtained from numerical simulations

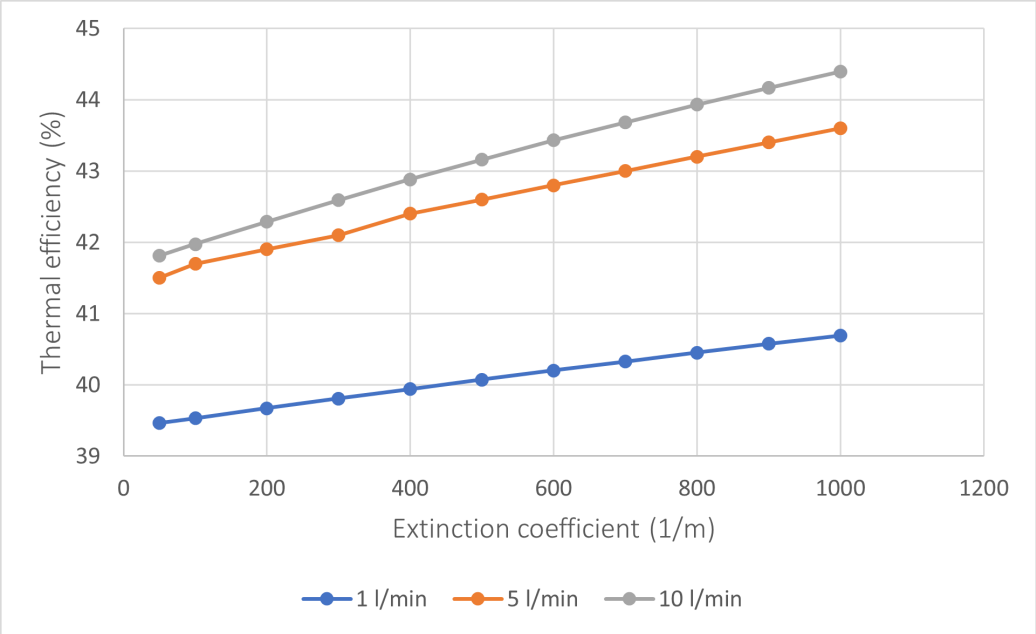

Figure 30: The thermal efficiency obtained from numerical simulations

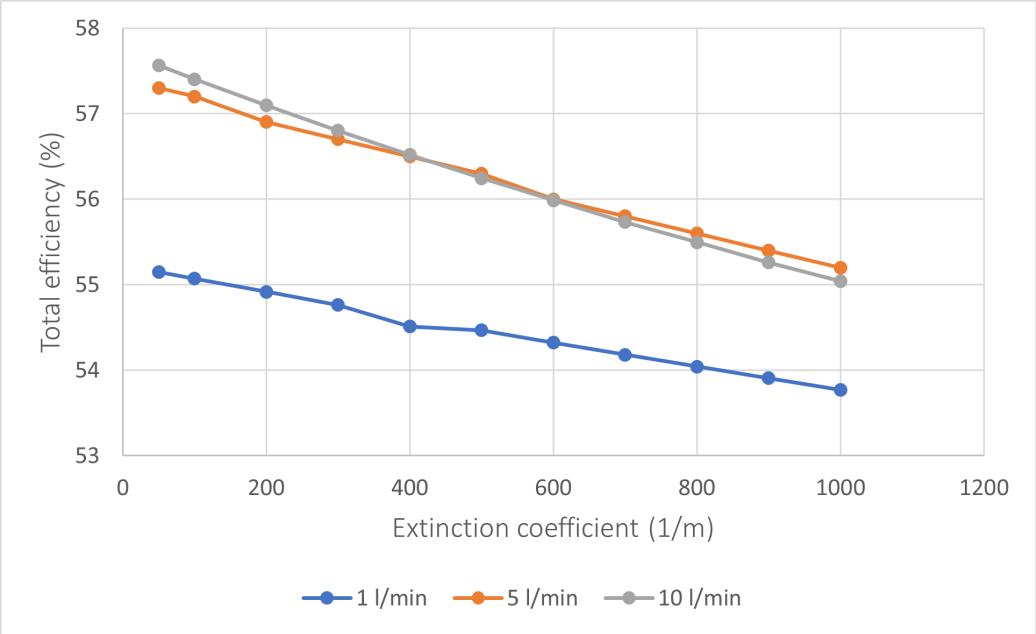

Figure 31: The total efficiency obtained from numerical simulations

Figure 29 shows how the electrical PV efficiency is affected by increasing the particle concentration for the different mass flow rates. The efficiency values are similar at the lower concentrations (0 – 0.001 wt.%). The coinciding values in this range of concentrations suggest that the electrical efficiency is not highly dependent on mass flow rate when the concentration is very low. Considering this result, increasing the flow rate would result in a higher cost for the system due to the increased pumping power.

It can be seen from the plot how the electrical efficiency decreases when the particle concentration is increased. The rate of decrease becomes higher when the flow rate is increased, so the lowest value (10.6 %) of electrical efficiency is achieved when the flow rate is 10 kg/min, and the particle concentration is 0.08 wt.%. This is a decrease of -8.2 % compared to the photovoltaic panel alone. The highest electrical efficiency (15.8 %) is found for the case associated with water when the flow rate is 5 kg/min. This is the same as the manufactured reference efficiency. However, it is an enhancement of 36.2 % compared to the numerically solved electrical efficiency of the photovoltaic panel alone, given in table 5.

Figure 30 shows how the modelled thermal efficiency is affected by increasing the particle concentration for the three different flow rates. First, one noticeable point is how close the plotted lines of 5 kg/min and 10 kg/min

lie to one another, as opposed to the plotted line of 1 kg/min. Increasing the flow rate from 1 to 5 kg/min results in a high jump in thermal efficiency, while further increasing it to 10 kg/min results in a much lower jump. At a very low mass flow rate, the fluid is exposed to radiation for longer, so it is expected to be more heated. However, the low flow rate also decreases relative to the photovoltaic panel and the surroundings, so the heat loss will, as expected, be higher. Also, because the heat transfer coefficient depends on the flow rate, it will be lower in this case, hence less heat flux between the panel and the fluid.

The same trend of thermal efficiency increasing proportionally to particle concentration is seen for all flow rates. As mentioned in Chapter 2.3.1, increasing the concentration in a nanofluid leads to higher radiation absorption, resulting in a higher fluid temperature due to the photothermal conversion. Equation (21) implies that the thermal efficiency is proportionally dependent upon the fluid outlet temperature. This explains the increased thermal efficiency. The highest thermal efficiency of 44.4 % is found when the flow rate is 10 kg/min, and the associated particle concentration is 0.08 wt.%. The lowest thermal efficiency, 39.5 %, corresponds to the case where pure water is considered, and the flow rate is 1 kg/min. Al-Shohani et al. [77] investigated a water-based PV/T system, and the highest achieved thermal efficiency of the system was 41.5 %, which only differs from the results of this project by 2 %. This suggests that the model used in this study is sufficient for the case of water.

Figure 31 shows how the total efficiency changes with the particle concentration. As for the thermal efficiency in figure 30, the plotted lines for 5 kg/min and 10 kg/min are roughly coinciding, even more for the total efficiency results. For mass concentrations from 0 to 0.014 wt.%, 10 kg/min is slightly more efficient than 5 kg/min. Between 0.014 wt.% and 0.027 wt.%, the two lines coincide. From 0.027 wt.% and up to 0.08 wt.%, 5 kg/min is the slightly more efficient flow rate. This means that doubling the flow rate leads to no remarkable efficiency enhancement. The highest total efficiency of 57.6 % corresponds to the case of water at a flow rate of 10 kg/min. The lowest total efficiency (53.7 %) of the system corresponds to the volume fraction of 0.08 wt.% and a mass flow rate of 1 kg/min. From the presented results for efficiencies, the system seems to be most efficient when the fluid applied is water. Considering the additional energy it takes to double the pumping power, the case of flow rate 5 kg/min might actually be the most efficient one.

Abdelrazik et al. [34] numerically investigated the effect of different operating

conditions in a PV/T with silver and water nanofluid as an optical filter. In this case, almost all the radiation in the range below the bandgap of the solar cell panel was absorbed. At low atmospheric temperature (25 °C), increasing the volume fraction of particles in the nanofluid resulted in decreasing electrical efficiency. The study explained the decrease by reduced transmission in the nanofluid. The same was discovered by Hjerrild et al. [33] when 0.088 wt.% carbon nanotubes from Sigma-Aldrich [78] dispersed in water were applied in an optical PV/T system. The nanofluid PV/T achieved higher thermal efficiency but lower electrical efficiency than for water. Similar results were achieved by He et al. [79], investigating Ag/TiO_2 nanoparticles in an optical PV/T system. This is similar to the behaviour of the numerically solved results in this study, with the same type of system.

Hjerrild et al. [33] also carried out the same study using core-shell Ag-SiO_2 particles in water, where concentrations 0.001 wt.% - 0.026 wt.% were considered. The study yielded a total efficiency enhancement of 30 %, compared to the case of using water. A composition of Ag-SiO_2 and carbon nanoparticles was also investigated in the system, resulting in reduced electrical efficiency. The high absorption explained the highest thermal efficiency values for the cases where carbon-based solutions were applied. On the other side, the highest electrical efficiency was achieved for the cases where no carbon-based nanofluid was applied.

For higher atmospheric temperature (45 °C), the electrical efficiency obtained by Abdelrazik et al. [34] did increase by increasing the particle fraction. Also, increasing solar concentration resulted in an increased electrical gain. This result suggests that the designed PV/T system is more efficient at higher temperatures and solar concentrations than the lower ones. This suggestion is also stated by Maadi et al. [18]. Because the solutions in this study are obtained at a low atmospheric temperature (20 °C), this can be part of the explanation for the decreasing electrical efficiency. By increasing the mass flow rate, Abdelrazik et al. [34] increased thermal and electrical efficiency. This is opposite to the results of this project, where increasing the mass flow rate decreases electrical efficiency. It is, however, important to note that the two studies investigate different types of nanofluids.

Crisostomo et al. [32] used core-shell Ag-SiO_2 particles in water as an optical filter for a PV/T system, where the electrical efficiency exhibited 9 % enhancement compared to the photovoltaic panel alone. The advantage of these particles is that the optical properties of the particles can easily be controlled by the thickness of the shell and the radius of the core, leading to a successful spectral splitting. Han et al. [80] experimentally investigated

a silver (Ag) and water-based PV/T system. The maximum electrical efficiency was obtained for the case with base fluid as an optical filter (8.8 %), which is lower than the manufactured photovoltaic efficiency (15.8 %). The thermal efficiency reached 79.4 %. The nanofluid exhibited good absorption for wavelengths below the PV bandgap range (325 - 670 nm) and good transmittance within the bandgap. Han et al. [81] also carried out a study for silver particles in $CoSO_4$ and water, yielding similar results. El-Samie et al. [82] did a numerical study on an optical PV/T system, considering Ag, Fe_3O_4 and SiO_2. Compared with the standalone PV, the total enhancement of the system ranged from 179 to 240 %.

Zhang et al. [83] studied a computational model of the energy enhancement of an optical nanofluid PV/T system. Silver was used as nanoparticle material, the height of the nanofluid channel was 5 mm, the mass flow rate was 0.3 l/min, and the inlet temperature was 25 °C. Beer-Lambert's law was applied to calculate transmittance in the nanofluid. When the mass flow rate is increased, so is the optical thickness. As discovered in this project, in figure 29, increasing the optical thickness leads to a decrease in electrical efficiency due to lower transmittance. This is because Beer-Lambert's law depends on the optical thickness, as seen in equation (18).

Stylianou [84] used CFD software to investigate a low concentration PV/T system. A case study resulted in thermal and electrical efficiencies of 84.6 % and 10.1 %, respectively. Compared to the results of this study, the electrical efficiency is about 5 % lower than the lowest electrical efficiency achieved. The optimized flow rate was reported to be 0.067 kg/s, corresponding to 4 kg/min. This is close to the optimal flow rate found in this study (5 kg/min). When the mass flow rate was doubled, the thermal output increased. The highest electrical efficiency is found in the case of the highest mass flow rate, 8 kg/min, which is not the case in this study. However, the highest electrical efficiency results for the simulated flow rates in this study are very close to one another.

As explained in Chapter 2.3.1, the extinction coefficients assigned to the different particle concentrations used in this project are assumed to be constant using the extinction coefficients measured by Struchalin et al. [37]. Trong et al. [85] investigated the radiation extinction of carbon-based nanofluids. For low concentrations, the extinction coefficients varied with wavelength. However, for example, at concentration 0.005 wt.%, the absorption became relatively high at all wavelengths, with slightly higher light transmission between 400 and 1400 nm. This implies that carbon-based nanofluids are more suitable for optical filtering at very low particle concentrations.

According to Gimeno-Furió et al. [86], the extinction coefficient of carbon-based nanofluid is a bit higher for the shorter wavelengths of the range. Because this is not accounted for in this project, the numerical model might have under-predicted the system's electrical efficiency. This is because if more of the radiation within the photovoltaic bandgap (700 - 1100 nm) is transmitted, the electrical generation will be higher. To obtain a more realistic numerical model of the PV/T system, it would be an idea to model the actual nanoparticles in the simulation, applying a multiphase flow model. The model might also be improved by accounting for varying absorption in the nanofluid at different incident wavelengths.

Another important note is that the model in this study does not include evaporation within the fluid, which is an essential factor considering heat transfer. Ni et al. [87] studied vapor generation within nanofluid in a solar receiver and how it affects several fluid properties. Findings could show that evaporation increased the heat transfer coefficient about ten times. Accounting for evaporation in the model of this study would possibly yield different results due to higher heat transfer between the domains. The heat transfer from the panel would possibly be higher, causing the electrical efficiency to increase. This would, however, lead to increased heat loss from the fluid, leading to lower thermal efficiency. Carbon black nanofluids generally have a higher rate of absorption than most metal-based nanofluids, and hence higher evaporation rate [88]. Therefore, it is crucial to consider this to obtain accurate results in a numerical model.

In other studies of optical PV/T systems, it seems that metal materials such as silver, especially core-shell nanoparticles, might be more suitable for this type of system due to their successful selective absorption. Several studies also exhibit good results when using water, in some cases even better than using nanofluids. There are several studies on PV/T systems with different approaches ([89], [18], [35], [90], [33], [34]). However, few studies focus on the operating conditions of a PV/T system and how they affect thermal and electrical performance.

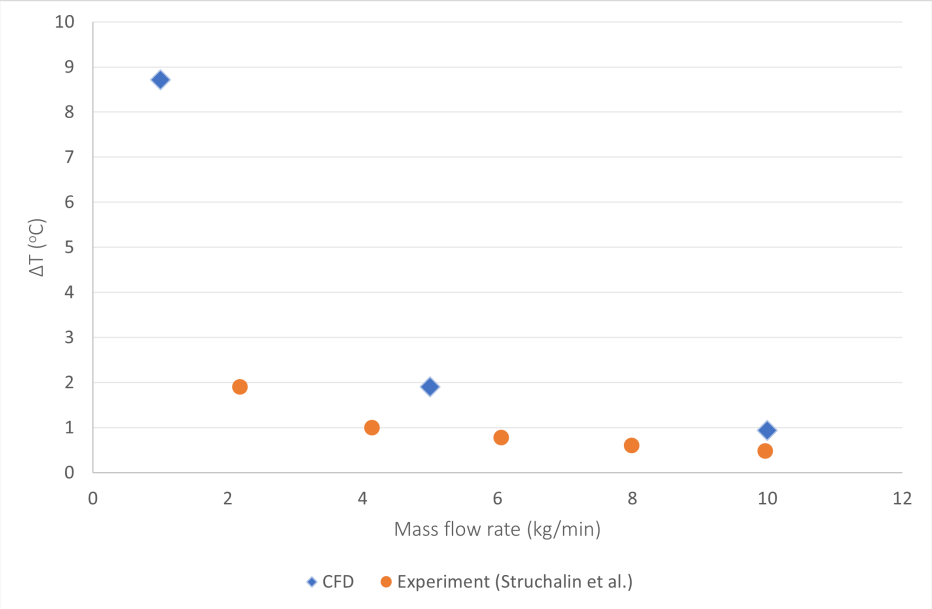

Figure 32: Temperature increase vs mass flow rate at concentration 0.01 wt.%

Figure 32 displays the simulated temperature difference between the fluid inlet and outlet versus the mass flow rate. For comparison, the experimental and computed results of Struchalin et al. [37] for a tubular DASC are included in the plot. It can be seen that the curves are similar in shape, where the slope is steep for the lower mass flow rates and flattens for increasing flow rates. In practice, this means that for high flow rates, the thermal efficiency becomes less dependent on the flow rate of the fluid. The same is suggested earlier in this chapter. However, it can be seen in figure 32 that the temperature increase is higher than for the case for the tubular DASC. Because this study's thin fluid film flow PV/T module differs significantly from a tubular DASC, the results will naturally differ.

4.2 Experimental Results

4.2.1 Nanofluid stability

The nanofluid preparation process faced challenges due to relatively low stability. After a day, there was significant and visible nanoparticle sediment at the bottom of the nanofluid container. This was the case for all concentrations (0.5 wt.% - 6 wt.%). For comparison, Struchalin et al. [37] observed no visible particle deposition in at least 45 days. However, this was the case for

much lower particle concentrations than those prepared in this project. The high concentration itself might be a reason for the unstable nanofluid. A possible solution to this problem might be increasing the amount of surfactant. Nonetheless, this solution might spark other problems when measuring thermal conductivity. When the concentration of SDS is too high, it might be difficult to know what dominates the thermal conductivity of the nanofluid, the surfactant, or the nanoparticles added to the water.

4.2.2 Thermal Conductivity

The measured values of the thermal conductivity is given in tables 13 - 16 in appendix B. T_s is the sonication duration in minutes, k_{avg} is the average of the measured thermal conductivity values, and n_{enh} is the percentage enhancement of thermal conductivity compared with the base fluid measured property. The measured thermal conductivity results from these tables are plotted in figure 33.

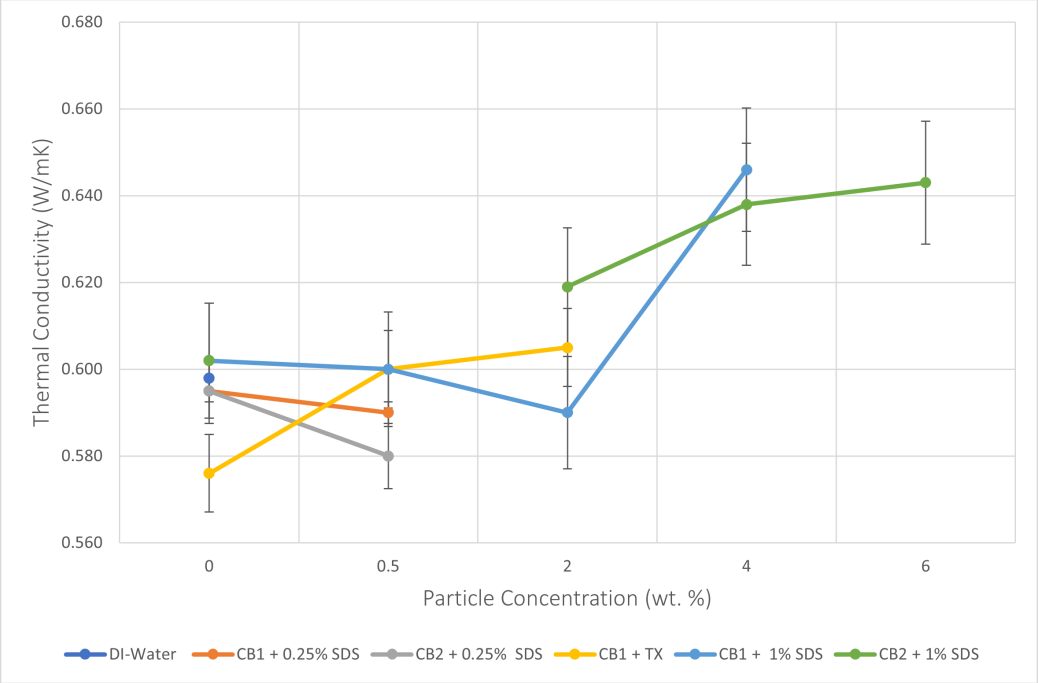

Figure 33: Measured thermal conductivity vs particle concentration

The results are somewhat scattered, but there is a general trend of increasing thermal conductivity for increasing particle concentration. This behaviour is expected, as mentioned in Chapter 2.3.2. However, some of the measured

values in tables 13 and 15 exhibit negative enhancement compared to the base fluid. As discussed in Chapter 2.3.2, the stability of the nanofluid is important for the thermal conductivity value. If particle agglomerates form within the nanofluid, it might cause instability and decreased thermal conductivity. Because the surface of the nanoparticles is not functionalized, this is a possible explanation for the negative enhancement. The uncertainty of the thermal conductivity measuring device is relatively high, and an important source of possibly inaccurate measurements.

In figure 34, some of the measured results from this study are plotted. To compare the results with the literature, the results from the study of Han et al. [89] are shown in the same figure. In their study, carbon black water-based nanofluid was prepared, and the thermal conductivity was measured. In the preparation process, the particles were functionalized, meaning they underwent a complicated process to enhance the stability of the nanofluid. The transient hot-wire method is used to measure the thermal conductivity, as in this study. The range of investigated particle concentrations was narrower, but it is explained in the study that the same trend can be expected for other concentrations. The slope of the curve from Han et al. is notably steeper than the one corresponding to this study. One possible explanation for this is the particle functionalization step in the other study, obtaining a more stable nanofluid than in this study. However, at concentrations between 2 and 3 wt.%, the results agree. Another experimental study of thermal conductivity of surface-modified multi-walled carbon nanotubes dispersed in water was carried out by Li et al. [51] for concentrations up to 5 wt.%. At particle concentrations 1 wt.% and 5 wt.%, the thermal conductivity was enhanced by 31.99 % and 69.7 %, respectively. This is a significantly higher enhancement than achieved in this study, giving more reason to believe that the modification step of the preparation process is vital to the results.

Hwang et al. [48] studied the thermal conductivity of multi-walled carbon nanotubes dispersed in water. The highest enhancement achieved was 11.3 % at concentration 2 wt.%, which is significantly higher than the corresponding results of this study. The increase of thermal conductivity seems to increase linearly up to 4 wt.% and flatten slightly up to 6 wt.%. This is possibly also connected to stability matters because, for very high concentrations, it is more difficult to obtain a stable nanofluid.

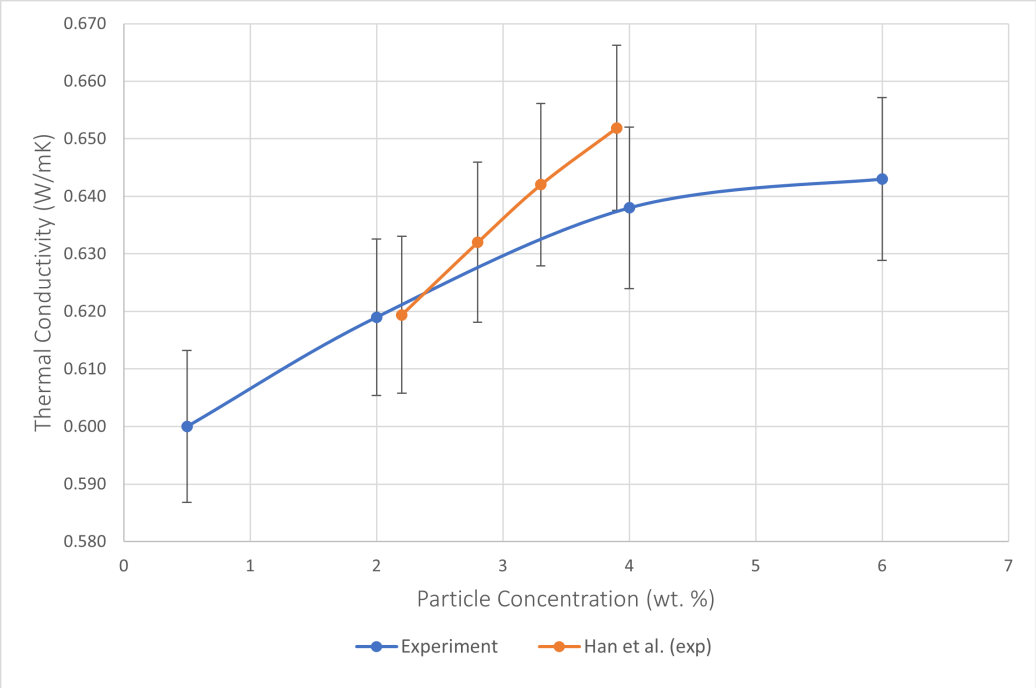

Figure 34: Chosen measured values of thermal conductivity from this study and Han et al. [89]

Fadhillahanafi et al. [91] conducted an experimental study measuring the thermal conductivity of multi-walled carbon nanotubes and water-based nanofluids, with and without surfactant (polyvinylpyrrolidone, PVP). For particle concentration 0.5 wt.% nanotubes and 0.01 wt.% PVP, the thermal conductivity was improved by 22.2 %. The highest measured enhancement at this particle concentration without surfactant in their study is 1.18 %, which is significantly lower. An important factor might be stability, and the study reported good nanofluid stability using PVP as a surfactant. The results prove the positive effect of using stabilizing additives in nanofluids to achieve high thermal conductivity.

As mentioned previously, Sedong et al. [45] did an experimental investigation of the thermal conductivity of various surfactants on graphene and carbon nanotube aqueous solutions. The surfactants studied were dodecyl benzene sulfonate (SDBS), sodium dodecyl sulfate (SDS), and dodecyl betaine (DB). Increasing the SDS concentration resulted in increased thermal conductivity. This can also be seen in table 13 from this study.

Table 16 shows that higher enhancement is achieved by increasing the power

of the ultrasonic device. In their experimental study on the stability of nanofluids, Sözen et al. [70] reported that the most effective dispersion power was 200 W. These results support the results of this study, where there is reported a significant enhancement for all the concentrations in table 16.

For the case where Triton X-100 is used as a surfactant, the nanofluid yields the highest enhancement value (5.07 %) for the particle concentration 2 wt.%. As mentioned in Chapter 3.2.2, the addition of Triton X-100 to a nanofluid results in higher stability and enhanced thermal conductivity ([22], [69], [71], [70]). However, some researchers state that for thermal conductivity enhancement matters, ionic surfactants like SDS are favourable. More research on this subject may be necessary.

5 Conclusion

In this project, an optical PV/T system was numerically investigated in a CFD model. The studied cases correspond to a standalone photovoltaic panel, a PV/T system with water, and a PV/T system with nanofluids using extinction coefficients of 50 to 1000 m^{-1}. The particle concentrations corresponding to the extinction coefficients were approximated according to the experimental results from Struchalin et al. [37]. The cases were simulated for the mass flow rates of 1, 5, and 10 kg/min. The electrical, thermal, and total efficiencies were numerically solved for each case and the results were discussed. This project also involved an experimental part, where high concentration carbon black nanofluids were prepared at 0.5 wt.% - 6 wt.%. Their thermal conductivity was measured using the transient hot-wire method.

The electrical efficiency that was found using the numerical modelling was the highest (15.8 %) for the case corresponding to water applied to the system. The value was achieved when the mass flow rate was set to 5 kg/min. Compared with the simulated case of the standalone photovoltaic panel, this corresponds to an electrical enhancement of 36.2 %. Increasing the extinction coefficient of the fluid in the model leads to a decreasing efficiency, agreeing with results from similar studies. The decrease can be explained by reduced transmission to the panel because of increased radiation absorption within the fluid. The lowest electrical efficiency, 10.6 %, was obtained when the flow rate was 10 kg/min, and the extinction coefficient was 1000 m^{-1}, corresponding to a particle concentration of 0.08 wt.%.

The opposite trend is discovered for the numerically calculated thermal efficiency of the system that increases with the extinction coefficient. The lowest thermal efficiency, 39.5 %, was obtained for water when the mass flow rate was set to 1 kg/min. The low absorption in the fluid can explain this result, and the low mass flow rate increases the heat loss. Decreasing the mass flow rate yields a lower heat transfer coefficient value, and the optical depth is lower. Both of these factors decrease the thermal performance of the fluid. The highest thermal efficiency can be seen for the mass flow rate of 10 kg/min, with an extinction coefficient associated with a particle concentration of 0.08 wt.%. In general, an increased mass flow rate results in a higher heat transfer coefficient and a thicker layer of fluid, hence this result is reasonable. Increasing the mass flow rate also means that the fluid's residence time in the collector is lower and it is therefore exposed to less heat loss. Lastly, the higher the particle concentration, the more heat will be absorbed in the fluid.

Concerning the total efficiency of the system, it can be observed that it decreases with increased particle concentration and decreased mass flow rate. The mass flow rates of 5 kg/min and 10 kg/min gave relatively similar results for the total efficiency, suggesting that the overall most efficient case corresponds to a mass flow rate of 5 kg/min. This suggestion can also be found in other studies, and doubling the flow rate will possibly only increase the power required by the system. The computational model yielded the optimal efficiency results when water was applied, as seen in other studies of a similar PV/T system.

Because some optical PV/T systems using other materials can show enhancement compared to water, it is reasonable to suggest that broadband absorbing material such as carbon black is not the most efficient in this type of PV/T system. The spectral filtering particles, such as core-shell nanoparticles consisting of metals and semiconducting materials, seem more suitable for an optical PV/T like this one. Carbon-based materials prove to be very efficient in direct absorption solar collectors and thermal PV/T systems because of their high radiative absorption. Also, carbon black exhibits impressive thermophysical properties, which are more prominent in these collectors and for higher particle concentrations.

Assumptions made in the modelled case are that the fluid is newtonian, steady temperature distribution, laminar and steady flow, and no drag force at the top layer of the fluid. In reality, several of these assumptions may be incorrect. There is, therefore, good reason to question the obtained results. However, the overall behaviour of the modelled case seems to agree well with other experimental and numerical investigations. Hence, the model can be a good starting point for numerical studies of PV/T systems. Due to the model's simplicity, it might be suitable for predicting trends and effects of changing the operational conditions. The model can be improved by advancing the numerical model to achieve more realistic results.

Considering the results from this project and the compared literature, it is safe to conclude that the optical PV/T yields an enhanced electrical efficiency compared to a simple photovoltaic panel. Water has proved to be the most efficient choice of fluid to use in this type of module. The advantage of applying a nanofluid in this PV/T system is the opportunity to control the optical and thermal properties of the fluid, which affects the amount of electrical and thermal output. This can, for example, be used to follow the demand for electricity and heat in a building.

It is challenging to obtain stable solutions when preparing high concentration carbon-based nanofluids. For particle concentrations 0.5 - 6 wt.%, there

was significant visible sediment after less than 24 hours, also when applying stabilizing additives such as Triton X-100 and SDS. The highest value of enhanced thermal conductivity, 7.38 %, is obtained for the nanofluid of particle concentration 4 wt.%. The literature shows significantly higher enhancement results for nanoparticles that have been functionalized before dispersing into the base fluid. There is reason to believe that the low enhancement is due to the missing stability of the nanofluid. However, the statement that increasing the particle concentration will increase the thermal conductivity agrees well with the results. When the particle concentration becomes relatively high, it is essential to obtain a stable nanofluid, or the thermal properties might only be negatively affected.

6 Future Work

Much research is available on the application of nanofluid in solar technology, especially for different types of flat-plate solar collectors. There is a number of studies on various material nanoparticles for different applications. However, there is less experimental and computational research on the application of nanofluids in optical PV/T systems. For the possibility of implementing this in commercial use, more research should be carried out. Further studies should include these key points:

- An optical nanofluid PV/T system with a high conentration of nanoparticles, where the flow of the nanofluid is dependent on the temperature of the photovoltaic panel
- The correlation between operational conditions and energy efficiency of the system,
- Ambient temperature and incident radiation intensity effect on the efficiency of the PV/T,
- A CFD-model accounting for the varying absorption of the solar spectrum, reflection, and the varying ambient temperature and incident radiation throughout the day,
- The relation of the optical thickness to the absorption in the fluid film,
- A study considering the economic feasibility of the optical nanofluid PV/T system.

References

[1] Energy production and consumption. [Online]. (Accessed: 20.04.2022). Available:https://ourworldindata.org/energy-production-consumption#how-much-energy-does-the-world-consume:.

[2] How have the world's energy sources changed over the last two centuries? [Online]. (Accessed: 02.05.2022). Available:https://ourworldindata.org/global-energy-200-years.

[3] Global electricity demand is growing faster than renewables, driving strong increase in generation from fossil fuels. [Online]. (Accessed: 20.04.2022). Available:https://www.iea.org/news/global-electricity-demand-is-growing-faster-than-renewables-driving-strong-increase-in-generation-from-fossil-fuels.

[4] World energy outlook 2021. [Online]. (Accessed: 11-12-2021). Available:https://iea.blob.core.windows.net/assets/888004cf-1a38-4716-9e0c-3b0e3fdbf609/WorldEnergyOutlook2021.pdf.

[5] S. K. Verma and A. K. Tiwari. Progress of nanofluid application in solar collectors: a review. *Energy Conversion and Management*, 100:324–346, 2015.

[6] IRENA. World energy transitions outlook 2022: 1.5° c pathway. 2021.

[7] How does solar work? [Online]. (Accessed: 14-12-2021). Available:https://www.energy.gov/eere/solar/how-does-solar-work.

[8] Spectral properties of sunlight. [Online]. (Accessed: 02.05.2022). Available:https://brilliant.org/practice/spectral-properties-sunlight/.

[9] Solar energy. [Online]. (Accessed: 03.05.2022). Available:https://www.irena.org/solar.

[10] Renewable energy. [Online]. (Accessed: 15-12-2021). Available:https://www.c2es.org/content/renewable-energy/.

[11] J. J. Michael, S. Iniyan, and R. Goic. Flat plate solar photovoltaic–thermal (pv/t) systems: a reference guide. *Renewable and sustainable energy reviews*, 51:62–88, 2015.

[12] J. Adeeb, A. Farhan, and A. Al-Salaymeh. Temperature effect on performance of different solar cell technologies. *Journal of Ecological Engineering*, 20(5), 2019.

[13] S. Hassani, R. A. Taylor, S. Mekhilef, and R. Saidur. A cascade nanofluid-based pv/t system with optimized optical and thermal properties. *Energy*, 112:963–975, 2016.

[14] Statistical review of world energy 2021. [Online]. (Accessed: 12-12-2021). Available:`https://www.bp.com/content/dam/bp/business-sites/en/global/corporate/pdfs/energy-economics/statistical-review/bp-stats-review-2021-at-a-glance.pdf`.

[15] O. Z. Sharaf, D. C. Kyritsis, A. N. Al-Khateeb, and E. Abu-Nada. Effect of bottom surface optical boundary conditions on nanofluid-based dasc: parametric study and optimization. *Solar Energy*, 164:210–223, 2018.

[16] M. Wolf. Performance analyses of combined heating and photovoltaic power systems for residences. *Energy Conversion*.

[17] P.G. Charalambous, G. G. Maidment, S. A. Kalogirou, and K. Yiakoumetti. Photovoltaic thermal (pv/t) collectors: A review. *Applied thermal engineering*, 27(2-3):275–286, 2007.

[18] S. R. Maadi, A. Navegi, E. Solomin, H. S. Ahn, S. Wongwises, and O. Mahian. Performance improvement of a photovoltaic-thermal system using a wavy-strip insert with and without nanofluids. *Energy*, page 121190, 2021.

[19] M. Gupta, V. Singh, R. Kumar, and Z. Said. A review on thermophysical properties of nanofluids and heat transfer applications. *Renewable and Sustainable Energy Reviews*, 74:638–670, 2017.

[20] S. Z. Heris, S. G. Etemad, and M. N. Esfahany. Experimental investigation of oxide nanofluids laminar flow convective heat transfer. *International communications in heat and mass transfer*, 33(4):529–535, 2006.

[21] S. U.S. Choi and J.A. Eastman. Enhancing thermal conductivity of fluids with nanoparticles. Technical report, Argonne National Lab.(ANL), Argonne, IL (United States), 1995.

[22] S. Hamze. *Graphene based nanofluids: development, characterization and application for heat and energy systems*. PhD thesis, Université Rennes 1, 2020.

[23] J. Lee, K. S. Hwang, S. P. Jang, B. H. Lee, J. H. Kim, S. U.S. Choi, and C. J. Choi. Effective viscosities and thermal conductivities of aqueous nanofluids containing low volume concentrations of al2o3 nanoparticles.

International Journal of Heat and Mass Transfer, 51(11-12):2651–2656, 2008.

[24] R.H. Davis. The effective thermal conductivity of a composite material with spherical inclusions. *International Journal of Thermophysics*, 7(3):609–620, 1986.

[25] L. Mahian, O.and Kolsi, M. Amani, P. Estellé, G. Ahmadi, C. Kleinstreuer, J. S. Marshall, M. Siavashi, R. A. Taylor, H. Niazmand, et al. Recent advances in modeling and simulation of nanofluid flows-part i: Fundamentals and theory. *Physics reports*, 790:1–48, 2019.

[26] R. A. Taylor, P. E. Phelan, T. P. Otanicar, R. Adrian, and R. Prasher. Nanofluid optical property characterization: towards efficient direct absorption solar collectors. *Nanoscale research letters*, 6(1):1–11, 2011.

[27] R. Taylor. *Thermal energy conversion in nanofluids*. Arizona State University, 2011.

[28] A. Kosinska, B.V. Balakin, and P. Kosinski. Use of biodegradable colloids and carbon black nanofluids for solar energy applications. *AIP Advances*, 11(5):055214, 2021.

[29] T. Yousefi, F. Veysi, E. Shojaeizadeh, and S. Zinadini. An experimental investigation on the effect of al2o3–h2o nanofluid on the efficiency of flat-plate solar collectors. *Renewable Energy*, 39(1).

[30] G. Colangelo, E. Favale, A. De Risi, and D. Laforgia. A new solution for reduced sedimentation flat panel solar thermal collector using nanofluids. *Applied Energy*, 111:80–93, 2013.

[31] H. Kim, J. Kim, and H. Cho. Experimental study on performance improvement of u-tube solar collector depending on nanoparticle size and concentration of al2o3 nanofluid. *Energy*, 118:1304–1312, 2017.

[32] F. Crisostomo, N. Hjerrild, S. Mesgari, Q. Li, and R. A. Taylor. A hybrid pv/t collector using spectrally selective absorbing nanofluids. *Applied energy*, 193:1–14, 2017.

[33] N. E. Hjerrild, S. Mesgari, F. Crisostomo, J. A. Scott, R. Amal, and R. A. Taylor. Hybrid pv/t enhancement using selectively absorbing ag–sio2/carbon nanofluids. *Solar Energy Materials and Solar Cells*, 147:281–287, 2016.

[34] A.S. Abdelrazik, R. Saidur, and F.A. Al-Sulaiman. Investigation of the performance of a hybrid pv/thermal system using water/silver nanofluid-based optical filter. *Energy*, 215:119172, 2021.

[35] A. N. Al-Shamani, M.A. Alghoul, A.M. Elbreki, A.A. Ammar, A. M. Abed, and K. Sopian. Mathematical and experimental evaluation of thermal and electrical efficiency of pv/t collector using different water based nano-fluids. *Energy*, 145:770–792, 2018.

[36] S. R. Abdallah, H. Saidani-Scott, and O. E. Abdellatif. Performance analysis for hybrid pv/t system using low concentration mwcnt (water-based) nanofluid. *Solar Energy*, 181:108–115, 2019.

[37] P.G. Struchalin, V.S. Yunin, K. V. Kutsenko, O.V. Nikolaev, A.A. Vologzhannikova, M.P. Shevelyova, O.S. Gorbacheva, and B.V. Balakin. Performance of a tubular direct absorption solar collector with a carbon-based nanofluid. *International Journal of Heat and Mass Transfer*, 179:121717, 2021.

[38] R.A. Taylor, T. Otanicar, and G. Rosengarten. Nanofluid-based optical filter optimization for pv/t systems. *Light: Science & Applications*, 1(10):e34–e34, 2012.

[39] A. Kosinska, B. V. Balakin, and P. Kosinski. Photothermal conversion of biodegradable fluids and carbon black nanofluids. 2021.

[40] Y. Hwang, J.K. Lee, C.H. Lee, Y.M. Jung, S.I. Cheong, C.G. Lee, B.C. Ku, and S.P. Jang. Stability and thermal conductivity characteristics of nanofluids. *Thermochimica Acta*, 455(1-2).

[41] K. Y. Leong, H. N. Mohd, S. R. Mohd, and N. H. Amer. The effect of surfactant on stability and thermal conductivity of carbon nanotube based nanofluids. *Thermal science*, 20(2):429–436, 2016.

[42] Y. Hwang, J. Lee, J. Lee, Y. Jeong, S. Cheong, Y. Ahn, and S.H. Kim. Production and dispersion stability of nanoparticles in nanofluids. *Powder Technology*, 186(2):145–153, 2008.

[43] E. T. Ulset, P. Kosinski, Y. Zabednova, O. V. Zhdaneev, P. G. Struchalin, and B. V. Balakin. Photothermal boiling in aqueous nanofluids. *Nano Energy*, 50:339–346, 2018.

[44] P.G. Struchalin, H. Thon, D.M. Kuzmenkov, K.V. Kutsenko, P. Kosinski, and B.V. Balakin. Solar steam generation enabled by iron oxide nanoparticles: Prototype experiments and theoretical model. *International Journal of Heat and Mass Transfer*, 158:119987, 2020.

[45] S. Kim, B. Tserengombo, S. Choi, J. Noh, S. Huh, B. Choi, H. Chung, J. Kim, and H. Jeong. Experimental investigation of dispersion characteristics and thermal conductivity of various surfactants on carbon based nanomaterial. *International Communications in Heat and Mass Transfer*, 91:95–102, 2018.

[46] T.P. Otanicar, P.E. Phelan, R.S. Prasher, G. Rosengarten, and R.A. Taylor. Nanofluid-based direct absorption solar collector. *Journal of renewable and sustainable energy*, 2(3):033102, 2010.

[47] M. Karami, M.A. Akhavan-Bahabadi, S. Delfani, and M. Raisee. Experimental investigation of cuo nanofluid-based direct absorption solar collector for residential applications. *Renewable and Sustainable Energy Reviews*, 52:793–801, 2015.

[48] Y.J. Hwang, Y.C. Ahn, H.S. Shin, C.G. Lee, G.T. Kim, H.S. Park, and J.K. Lee. Investigation on characteristics of thermal conductivity enhancement of nanofluids. *Current Applied Physics*, 6(6):1068–1071, 2006.

[49] Y. Yang, Z. G. Zhang, E. A. Grulke, W. B. Anderson, and G. Wu. Heat transfer properties of nanoparticle-in-fluid dispersions (nanofluids) in laminar flow. *International journal of heat and mass transfer*, 48(6):1107–1116, 2005.

[50] J. J. G. Bester et al. *Carbon black nanofluid synthesis for use in concentrated solar power applications*. PhD thesis, University of Pretoria, 2016.

[51] X. Li, W. Chen, and C. Zou. The stability, viscosity and thermal conductivity of carbon nanotubes nanofluids with high particle concentration: A surface modification approach. *Powder Technology*, 361:957–967, 2020.

[52] W. L. McCabe, Julian C. Smith, and P. Harriott. *Unit operations of chemical engineering*, volume 5. McGraw-hill New York, 1993.

[53] W. M. Rohsenow, J. P. Hartnett, Y. I. Cho, et al. *Handbook of heat transfer*, volume 3. McGraw-Hill New York, 1998.

[54] Solar radiation basics. [Online]. (Accessed: 06.05.2022). Available:`https://www.energy.gov/eere/solar/solar-radiation-basics`.

[55] Energy of photon. [Online]. (Accessed: 06.05.2022). Available:`https://www.pveducation.org/pvcdrom/properties-of-sunlight/energy-of-photon`.

[56] Solar spectrum. [Online]. (Accessed: 12.05-2022). Available:https://commons.wikimedia.org/wiki/File:Solar_Spectrum.png.

[57] A.J. Hunt. Small particle heat exchangers. Technical report, California Univ., Berkeley (USA). Lawrence Berkeley Lab., 1978.

[58] P. Andresen, A. Bath, W. Gröger, H.W. Lülf, G. Meijer, and J.J. Ter Meulen. Laser-induced fluorescence with tunable excimer lasers as a possible method for instantaneous temperature field measurements at high pressures: checks with an atmospheric flame. *Applied Optics*, 27(2):365–378, 1988.

[59] M. Chandrasekar, S. Suresh, and A. Ch. Bose. Experimental investigations and theoretical determination of thermal conductivity and viscosity of al2o3/water nanofluid. *Experimental Thermal and Fluid Science*, 34(2):210–216, 2010.

[60] S. Lee, S.U.S. Choi, S. Li, , and J.A. Eastman. Measuring thermal conductivity of fluids containing oxide nanoparticles. 1999.

[61] H. Masuda, A. Ebata, and K. Teramae. Alteration of thermal conductivity and viscosity of liquid by dispersing ultra-fine particles. dispersion of al2o3, sio2 and tio2 ultra-fine particles. 1993.

[62] What is cfd — computational fluid dynamics? [Online]. (Accessed: 01-12-2021). Available:https://www.simscale.com/docs/simwiki/cfd-computational-fluid-dynamics/what-is-cfd-computational-fluid-dynamics/.

[63] J. D. Anderson and J. Wendt. *Computational fluid dynamics*, volume 206. Springer, 1995.

[64] Siemens Software Simcenter. *STAR-CCM+ User guide for version 15.02.007*. (Accessed: 22.04.2022).

[65] Rec peak energy series. [Online]. (Accessed: 15-09-2021). Available:https://www.energymatters.com.au/images/rec-solar/rec-peak-energy.pdf.

[66] A. Seeni, P. Rajendran, and H. Mamat. A cfd mesh independent solution technique for low reynolds number propeller. 2021.

[67] Carbon nanofiber. [Online]. (Accessed: 01-02-2022). Available:https://bergencarbonsolutions.com/product/.

[68] Timcal ensaco™ 350g conductive carbon black. [Online]. (Accessed: 24.04.2022). Available:https://www.matweb.com/search/datasheet.aspx?matguid=bd030f9e04044d2c90d11568a129e8db.

[69] M.J. Assael, I.N. Metaxa, K. Kakosimos, and D. Constantinou. Thermal conductivity of nanofluids-experimental and theoretical. *International Journal of Thermophysics*, 27(4):999–1017, 2006.

[70] A. Sözen, M. Gürü, T. Menlik, U. Karakaya, and E. Çiftçi. Experimental comparison of triton x-100 and sodium dodecyl benzene sulfonate surfactants on thermal performance of tio2–deionized water nanofluid in a thermosiphon. *Experimental Heat Transfer*, 31(5):450–469, 2018.

[71] M. Mehrali, E. Sadeghinezhad, S. Tahan Latibari, M. Mehrali, H. Togun, M.N.M. Zubir, S.N. Kazi, and H.S.C. Metselaar. Preparation, characterization, viscosity, and thermal conductivity of nitrogen-doped graphene aqueous nanofluids. *Journal of materials science*, 49(20):7156–7171, 2014.

[72] Mettler toledo. [Online]. (Accessed: 09.05.2022). Available:https://www.mt.com/no/no/home.html.

[73] Up200ht – handheld ultrasonic homogenizer. [Online]. (Accessed: 24.04.2022). Available:https://www.hielscher.com/200ht_p.htm.

[74] Y. Hwang, H.S. Park, J.K. Lee, and W.H. Jung. Thermal conductivity and lubrication characteristics of nanofluids. *Current Applied Physics*, 6:e67–e71, 2006.

[75] S.A. Angayarkanni and J. Philip. Review on thermal properties of nanofluids: Recent developments. *Advances in colloid and interface science*, 225:146–176, 2015.

[76] Managing errors and uncertainty. [Online]. (Accessed: 21.05.2022). Available:https://www.physics.upenn.edu/sites/default/files/Managing\%20Errors\%20and\%20Uncertainty.pdf.

[77] W.A.M. Al-Shohani, R. Al-Dadah, and S. Mahmoud. Reducing the thermal load of a photovoltaic module through an optical water filter. *Applied Thermal Engineering*, 109:475–486, 2016.

[78] Carbon nanotube, multi-walled. [Online]. (Accessed: 28.04.2022). Available:https://www.sigmaaldrich.com/NO/en/search/carbon-nanotube?focus=products&page=1&perpage=30&sort=relevance&term=carbon\%20nanotube&type=product_name.

[79] Y. He, Y. Hu, and H. Li. An ag@ tio2/ethylene glycol/water solution as a nanofluid-based beam splitter for photovoltaic/thermal applications in cold regions. *Energy Conversion and Management*, 198:111838, 2019.

[80] X. Han, X. Chen, Y. Sun, and J. Qu. Performance improvement of a pv/t system utilizing ag/coso4-propylene glycol nanofluid optical filter. *Energy*, 192:116611, 2020.

[81] X. Han, X. Chen, Q. Wang, S. M. Alelyani, and J. Qu. Investigation of coso4-based ag nanofluids as spectral beam splitters for hybrid pv/t applications. *Solar Energy*, 177:387–394, 2019.

[82] Mostafa M Abd El-Samie, Xing Ju, Chao Xu, Xiaoze Du, and Qunzhi Zhu. Numerical study of a photovoltaic/thermal hybrid system with nanofluid based spectral beam filters. *Energy Conversion and Management*, 174:686–704, 2018.

[83] C. Zhang, C. Shen, Y. Zhang, and J. Pu. Feasibility investigation of spectral splitting photovoltaic/thermal systems for domestic space heating. *Renewable Energy*, 2022.

[84] S. Stylianou. Thermal simulation of low concentration pv/thermal system using a computational fluid dynamics software. 2016.

[85] N. Trong Tam, N. Viet Phuong, P. Hong Khoi, P. Ngoc Minh, M. Afrand, P. Van Trinh, B. Hung Thang, G. Żyła, and P. Estellé. Carbon nanomaterial-based nanofluids for direct thermal solar absorption. *Nanomaterials*, 10(6):1199, 2020.

[86] A. Gimeno-Furió, R. Martínez-Cuenca, R. Mondragón, A. F. V. Gasulla, C. Doñate-Buendía, G. Mínguez-Vega, and L. Hernández. Optical characterisation and photothermal conversion efficiency of a water-based carbon nanofluid for direct solar absorption applications. *Energy*, 212:118763, 2020.

[87] G. Ni, N. Miljkovic, H.. Ghasemi, X. Huang, S.V. Boriskina, C. Lin, J. Wang, Y. Xu, M.M. Rahman, T. Zhang, et al. Volumetric solar heating of nanofluids for direct vapor generation. *Nano Energy*, 17:290–301, 2015.

[88] A. Zeiny, H. Jin, G. Lin, P. Song, and D. Wen. Solar evaporation via nanofluids: A comparative study. *Renewable Energy*, 122:443–454, 2018.

[89] D. Han, Z. Meng, D. Wu, C. Zhang, and H. Zhu. Thermal properties of carbon black aqueous nanofluids for solar absorption. *Nanoscale research letters*, 6(1):1–7, 2011.

[90] R. Daghigh, M. H. Ruslan, and K. Sopian. Advances in liquid based photovoltaic/thermal (pv/t) collectors. *Renewable and Sustainable Energy Reviews*, 15(8):4156–4170, 2011.

[91] N.M. Fadhillahanafi, K.Y. Leong, and M.S. Risby. Stability and thermal conductivity characteristics of carbon nanotube based nanofluids. *International Journal of Automotive & Mechanical Engineering*, 8, 2013.

Appendices

A Computational Fluid Dynamics Results

A.1 Model Validation

T_w(°C)	T_{theory} (°C)	$T_{numerical}$(°C)
10	10.4	10.0
15	15.2	15.0
20	20.0	20.0
30	29.6	30.0
40	39.1	40.0
50	48.7	50.0
60	58.3	60.0

Table 6: Constant wall temperature and theoretically and numerically solved fluid outlet temperatures

A.2 Mesh Independence Results

Prism layer total thickness (m)	$\mid \delta_{theoretical} - \delta_{sim} \mid$ (10^{-6} m)
0.00075	1.51592
0.00150	1.29128
0.00225	1.29362
0.00300	1.29525
0.00375	1.29589
0.00450	1.36596

Table 7: Absolute difference between expected and simulated value of fluid film thickness

Number of prism layers	$\mid \delta_{theoretical} - \delta_{sim} \mid (10^{-6}\text{m})$
1	1.28928
2	1.29128
3	1.29167
4	1.29184
5	1.29193
6	1.29198

Table 8: Absolute difference between expected and simulated value of fluid film thickness, varying the prism layer total thickness

Base size (m)	$\mid \delta_{theoretical} - \delta_{sim} \mid (10^{-6}\text{m})$
0.02	1.38288
0.03	1.23166
0.04	1.19613
0.05	1.16101
0.06	1.32764
0.07	1.32764

Table 9: Absolute difference between expected and simulated value of fluid film thickness, varying the base size

A.3 Efficiency Results

σ (m^{-1})	$\eta_{electrical}$ (%)	$\eta_{thermal}$ (%)	η_{total} (%)
50	15.7	39.5	55.2
100	15.5	39.5	55.1
200	15.3	39.7	54.9
300	14.9	39.8	54.8
400	14.6	39.9	54.5
500	14.4	40.1	54.5
600	14.1	40.2	54.3
700	13.9	40.3	54.2
800	13.6	40.5	54.0
900	13.3	40.6	53.9
1000	13.1	40.7	53.8

Table 10: Electrical, thermal and total efficiency simulated for different extinction coefficients for mass flow rate 1 kg/min

σ (m^{-1})	$\eta_{electrical}$ (%)	$\eta_{thermal}$ (%)	η_{total} (%)
50	15.8	41.5	57.3
100	15.5	41.7	57.2
200	15.0	41.9	56.9
300	14.6	42.1	56.7
400	14.1	42.4	56.5
500	13.7	42.6	56.3
600	13.2	42.8	56.0
700	12.8	43.0	55.8
800	12.4	43.2	55.6
900	12.0	43.4	55.4
1000	11.6	43.6	55.2

Table 11: Electrical, thermal and total efficiency simulated for different extinction coefficients for mass flow rate 5 kg/min

σ (m^{-1})	$\eta_{electrical}$ (%)	$\eta_{thermal}$ (%)	η_{total} (%)
50	15.8	41.8	57.6
100	15.4	42.0	57.4
200	14.8	42.3	57.1
300	14.2	42.6	56.8
400	13.6	42.9	56.5
500	13.1	43.2	56.2
600	12.6	43.4	56.0
700	12.1	43.7	55.7
800	11.6	43.9	55.5
900	11.1	44.2	55.3
1000	10.7	44.4	55.0

Table 12: Electrical, thermal and total efficiency simulated for different extinction coefficients for mass flow rate 10 kg/min

B Thermal Conductivity Measurements

CB wt.%	ΔCB (10^{-5})	SDS wt.%	ΔSDS (10^{-5})	T_s	k_{avg}	Δk	n_{enh}
0		1	3.33	40	0.602	0.013	0
0.5	3.33	1	3.33	40	0.600	0.013	-0.20
2	3.34	1	3.33	120	0.590	0.014	0.57
4	3.34	1	3.33	120	0.646	0.014	7.38
0		0.25	3.33	40	0.595	0.013	0
0.5	3.33	0.25	3.33	40	0.587	0.013	-1.38
0.5	3.33	0.25	3.33	120	0.590	0.013	-0.59

Table 13: Measured values of thermal conductivity for the carbon nanofibers [67] with water and SDS (Power = 50 W)

CB wt.%	ΔCB (10^{-5})	TX-100 wt.%	ΔTX (10^{-5})	T_s	k_{avg}	Δk	n_{enh}
0		1	3.33	0	0.576	0.013	0
0.5	3.33	1	3.33	40	0.600	0.014	1.18
2	3.34	1	3.33	120	0.605	0.014	5.07

Table 14: Thermal conductivity for the carbon nanofibers [67] with water and Triton X-100 (Power = 50 W)

CB wt.%	ΔCB (10^{-5})	SDS wt.%	ΔSDS (10^{-5})	T_s	k_{avg}	Δk	n_{enh}
0.5	3.33	0.25	3.33	120	0.580	0.013	-2.65
2	3.34	1	3.33	120	0.579	0.013	-3.69

Table 15: Thermal conductivity for the spherical carbon naoparticles (Timcal Ensaco 350g) [68] with water and SDS (Power = 50 W)

CB wt.%	ΔCB (10^{-5})	SDS wt.%	ΔSDS (10^{-5})	T_s	k_{avg}	Δk	n_{enh}
2	3.34	1	3.33	60	0.619	0.014	2.96
4	3.34	1	3.33	60	0.638	0.014	6.12
6	3.35	1	3.33	60	0.643	0.014	6.88

Table 16: Thermal conductivity for the spherical carbon naoparticles (Timcal Ensaco 350g) [68] with water and SDS (Power = 200 W)